Monthly Notices of the ROYAL ASTRONOMICAL SOCIETY

MNRAS **528,** 1863–1878 (2024) https://doi.org/10.1093/mnras/stae026
Advance Access publication 2024 January 27

A cooling flow around the low-redshift quasar H1821+643

H. R. Russell,[1]★ P. E. J. Nulsen,[2,3] A. C. Fabian,[4] T. E. Braben,[1] W. N. Brandt,[5,6,7] L. Clews,[1,8] M. McDonald,[9,10] C. S. Reynolds,[11,12] J. S. Sanders[13] and S. Veilleux[11,12]

[1]*School of Physics & Astronomy, University of Nottingham, University Park, Nottingham NG7 2RD, UK*
[2]*Center for Astrophysics | Harvard & Smithsonian, 60 Garden Street, Cambridge, MA 02138, USA*
[3]*ICRAR, University of Western Australia, 35 Stirling Hwy, Crawley, WA 6009, Australia*
[4]*Institute of Astronomy, Madingley Road, Cambridge CB3 0HA, UK*
[5]*Department of Astronomy & Astrophysics, 525 Davey Lab, The Pennsylvania State University, University Park, PA 16802, USA*
[6]*Institute for Gravitation and the Cosmos, The Pennsylvania State University, University Park, PA 16802, USA*
[7]*Department of Physics, 104 Davey Lab, The Pennsylvania State University, University Park, PA 16802, USA*
[8]*School of Physical Sciences, The Open University, Walton Hall, Milton Keynes MK7 6AA, UK*
[9]*Department of Physics, Massachusetts Institute of Technology, Cambridge, MA 02139, USA*
[10]*Kavli Institute for Astrophysics and Space Research, Massachusetts Institute of Technology, 77 Massachusetts Avenue, Cambridge, MA 02139, USA*
[11]*Department of Astronomy, University of Maryland, College Park, MD 20742-2421, USA*
[12]*Joint Space-Science Institute (JSI), College Park, MD 20742-2421, USA*
[13]*Max-Planck-Institut für extraterrestrische Physik, Gießenbachstraße 1, D-85748, Garching, Germany*

Accepted 2023 December 19. Received 2023 December 11; in original form 2023 October 20

ABSTRACT

H1821+643 is the nearest quasar hosted by a galaxy cluster. The energy output by the quasar, in the form of intense radiation and radio jets, is captured by the surrounding hot atmosphere. Here, we present a new deep *Chandra* observation of H1821+643 and extract the hot gas properties into the region where Compton cooling by the quasar radiation is expected to dominate. Using detailed simulations to subtract the quasar light, we show that the soft-band surface brightness of the hot atmosphere increases rapidly by a factor of ∼30 within the central ∼10 kpc. The gas temperature drops precipitously to < 0.4 keV and the density increases by over an order of magnitude. The remarkably low metallicity here is likely due to photoionization by the quasar emission. The variations in temperature and density are consistent with hydrostatic compression of the hot atmosphere. The extended soft-band peak cannot be explained by an undersubtraction of the quasar or scattered quasar light and is instead due to thermal interstellar medium. The radiative cooling time of the gas falls to only 12 ± 1 Myr, below the free fall time, and we resolve the sonic radius. H1821+643 is therefore embedded in a cooling flow with a mass deposition rate of up to 3000 $M_\odot$ yr^{-1}. Multiwavelength observations probing the star-formation rate and cold gas mass are consistent with a cooling flow. We show that the cooling flow extends to much larger radii than can be explained by Compton cooling. Instead, the active galactic nucleus appears to be underheating the core of this cluster.

Key words: intergalactic medium – quasars: individual: H1821+643 – X-rays: galaxies: clusters.

1. INTRODUCTION

Accretion on to supermassive black holes (SMBHs) powers the intense radiation and winds observed in distant quasars and spectacular relativistic jets in radio galaxies that can reach far beyond the host galaxy. This energy input is now understood to be the key mechanism in structure formation that truncates the growth of massive galaxies and suppresses cooling flows at the centres of rich galaxy clusters (e.g. Bower et al. 2006; Croton et al. 2006; Hopkins et al. 2006 and for a review see Fabian 2012). The clearest observational evidence for this mechanism is found in nearby galaxy clusters, where the energy output by the central active galactic nucleus (AGN) is imprinted on the hot atmosphere. In these systems, radio jets launched by the SMBH carve out huge cavities and drive a series of weak shocks and sound waves into the hot gas (e.g. Fabian et al. 2000, 2006; McNamara et al. 2000 and for a review see McNamara & Nulsen 2007). The radio jets and lobes expand against the pressure of the hot atmosphere; therefore the minimum energy input is given by $4pV$, where p is the gas pressure and the cavity volume V is based on the extent on the sky (e.g. Churazov et al. 2002). The captured energy replaces the substantial radiative losses from the cluster's atmosphere, which would otherwise cool rapidly and flood the central galaxy with cold gas (a cooling flow, Fabian 1994). This radio or maintenance-mode of feedback is thought to suppress gas cooling and star formation in massive galaxies and clusters at late times in the Universe.

At high redshift, higher accretion rates on to these SMBHs fuelled a radiatively efficient quasar-mode of feedback. In this mode, intense radiation and high-velocity winds generated close to

★ E-mail: helen.russell@nottingham.ac.uk

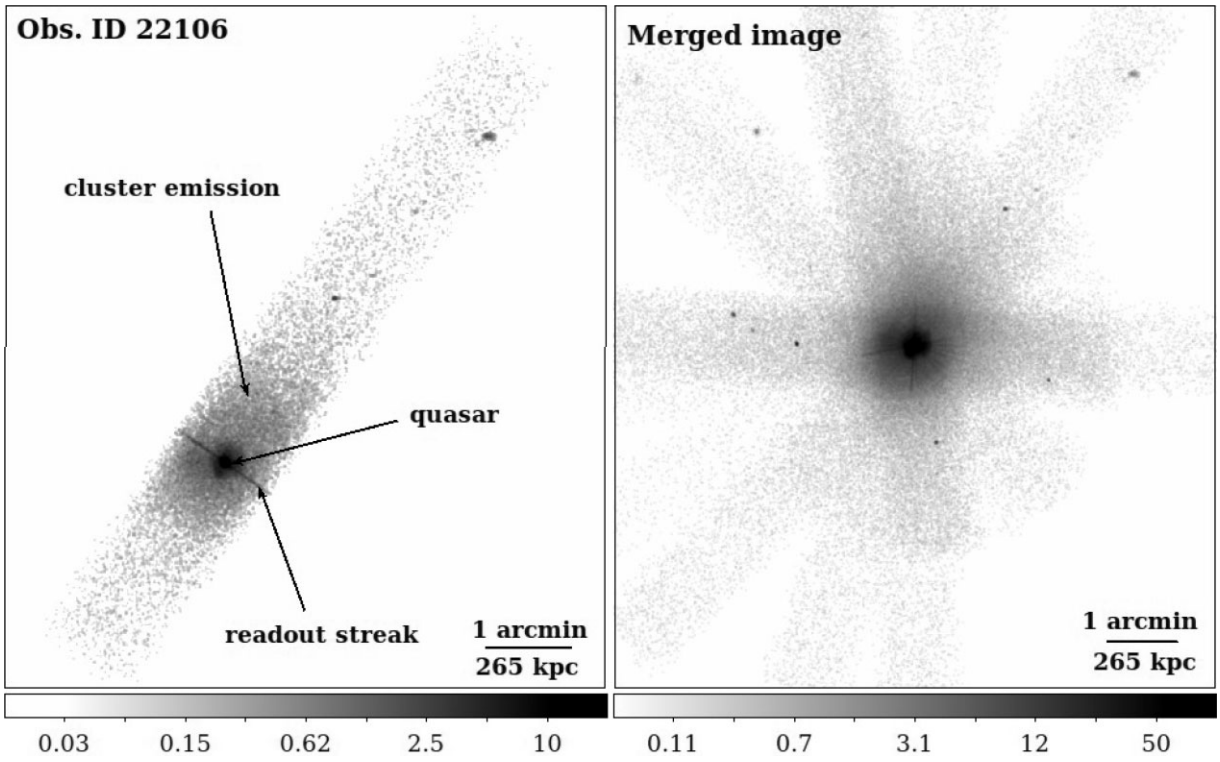

Figure 1. Left panel: Image for a single *Chandra* observation of H1821+643 showing the 1/8 subarray and readout streak from the bright quasar (Obs. ID 22106). Right panel: Image showing all data sets merged. The range of roll angles for the separate observations changes the orientation of the CCD and readout streak. Images have units of counts, cover the energy range 0.5−7 keV, and were smoothed with a 2D Gaussian with $\sigma = 1.5$ arcsec.

the quasar shock-heat and expel the surrounding gas and prevent further gas inflow (e.g. Di Matteo, Springel & Hernquist 2005; King & Pounds 2015). Quasar-mode feedback was probably most effective and prevalent at the height of quasar activity at $z \sim 2$–3, when galaxies were most gas-rich and intensively forming stars. By driving outflows and depleting the fuel supply, quasar-mode feedback would produce the observed decline in activity from both black holes and star formation and push galaxies on to the $M_{\rm BH}$–σ relation. However, detailed studies of the impact of these powerful quasars on hot atmospheres have so far been limited by the lack of suitable low-redshift analogues. Only two are known in the local universe ($z < 0.5$): H1821+643 ($z = 0.299$; Russell et al. 2010) and CL09104+4109, which is highly obscured ($z = 0.44$; O'Sullivan et al. 2012).

The massive galaxy cluster surrounding the quasar H1821+643 is optically rich and has an X-ray bright, strong cool core. The quasar has a bolometric luminosity of $\sim 10^{47}$ erg s^{-1} and this nuclear emission dominates over that from the hot gas within the central few arcsec (Fang et al. 2002). A deep Very Large Array (VLA) observation revealed that, although classified as a radio-quiet quasar (based on the 5 GHz luminosity of $10^{23.9}$ W Hz^{-1} sr^{-1}), H1821+643 hosts a giant 300 kpc Fanaroff–Riley type I radio source (Blundell & Rawlings 2001).Previous *Chandra* imaging observations suggest complex interplay between the AGN activity and the surrounding cluster gas (Russell et al. 2010). Bright arms of cool gas extend along the radio lobes and around the rim of an X-ray cavity. Using detailed point spread function (PSF) simulations to subtract the quasar emission, Russell et al. (2010) extracted the underlying temperature and density profiles of the hot atmosphere. The gas temperature drops steadily from 10 keV at ∼80 kpc to 2 keV at 20 kpc. When compared with other strong cool core clusters, the resulting entropy profile for H1821+643 has a significantly steeper decline within the central ∼80 kpc (Walker et al. 2014). The quasar may have a marked cooling effect on the surrounding hot gas, likely through Compton scattering, which would also boost the accretion rate on to the SMBH and extend this burst of quasar activity (Fabian & Crawford 1990). However, heavy pile-up of the quasar emission in the previous *Chandra* observations (> 80 per cent of photons affected) ultimately prevented us from extracting the underlying hot gas properties into the region where Compton cooling is expected to dominate.

Here, we present a new deep *Chandra* observation of H1821+643 taken with a short frame-time of 0.4 s to minimize pile-up and allow us to measure the temperature and density of the hot gas within the central 20 kpc. In Sections 2 and 3, we discuss the data reduction, pile-up, and the detailed simulation and subtraction of the quasar PSF. Section 4 examines the morphology of the underlying hot atmosphere and Section 5.1 maps the gas properties using spatially resolved spectroscopy. Finally, in Section 6, we discuss the evidence for and origin of the cooling flow at the centre of H1821+643. We assume $H_0 = 70$ km s^{-1} Mpc^{-1}, $\Omega_{\rm m} = 0.3$, and $\Omega_\Lambda = 0.7$, translating to a scale of 4.4 kpc per arcsec at the redshift $z = 0.296$ of H1821+643 (Monroe et al. 2016). All errors are 1σ unless otherwise noted.

2. DATA REDUCTION

H1821+643 was observed by *Chandra* with the ACIS-S detector for a total of 582 ks split over 22 separate observations between 2019 October and 2020 September (Fig. 1). The bright quasar was positioned 1 arcmin off-axis to ensure the field of view covered the galaxy cluster core. *Chandra* does not have a shutter so quasar photons arriving during CCD readout produce a clear readout streak

Table 1. Details of the new *Chandra* observations analysed in this work.

Date	Obs. ID	Aim point	Exposure (ks)	Date	Obs. ID	Aim point	Exposure (ks)
2019 Oct 7	22105	S3	36.3	2020 July 18	23319	S3	20.4
2019 Oct 23	22106	S3	45.4	2020 July 19	23239	S3	39.1
2019 Dec 28	23054	S3	41.8	2020 Aug 7	22104	S3	20.9
2020 Apr 10	21559	S3	25.5	2020 Aug 9	23339	S3	14.6
2020 Apr 10	23211	S3	18.2	2020 Aug 22	23053	S3	22.7
2020 Apr 20	21558	S3	42.7	2020 Sep 16	22103	S3	13.7
2020 May 8	21561	S3	24.1	2020 Sep 18	22109	S3	22.7
2020 May 10	23240	S3	22.7	2020 Sep 19	24612	S3	27.6
2020 May 28	22108	S3	13.7	2020 Sep 24	24639	S3	30.9
2020 June 20	22107	S3	34.4	2020 Sep 26	24641	S3	22.7
2020 July 15	21560	S3	32.7	2020 Sep 27	24661	S3	9.1

across the detector. All observations were taken with a 1/8 subarray and reduced frame-time of 0.4 s to minimize pile-up. Pile-up occurs when multiple photons arrive in the same pixel within a single ACIS frame integration time (typically 3.1 s). These photons are detected as a single event of higher energy and with an extended charge cloud distribution. An event with an extended charge cloud distribution is more likely to be flagged as a background event and excluded from analysis. Pile-up therefore hardens the source spectrum and reduces the detected flux. Pile-up can be reduced by reducing the frame-time; however, this requires faster readout so the CCD area must be decreased by using a subarray.

Using PIMMS (Mukai 1993), we estimated that $\sim$25 per cent of quasar photons are piled up in the new observations. Whilst far below the $>$ 80 per cent pile-up predicted for a frame-time of 3.1 s, this is still sufficient to reduce the measured count rate from 1.8 cts s^{-1} to 1.0 cts s^{-1} and produce a coincident peak in bad event grades. Based on the ratio of bad to good grades, pile-up predominantly affects the very centre of the quasar's PSF within 1 arcsec. We note that mild pile-up ($<$ 5 per cent) is also found from 1$-$2 arcsec, which is considered when analysing the radial profiles for the extended emission.

The data sets were reduced and analysed with CIAO version 4.14 and CALDB version 4.9.8 provided by the *Chandra* X-ray Center (CXC; Fruscione et al. 2006). The latest gain and charge transfer inefficiency correction were applied and the event files were filtered for bad grades. For this analysis, the improved background screening available from VFAINT mode was not applied to minimize loss of piled-up photons. Background light curves were extracted from the outskirts of the CCD and filtered with the LC_CLEAN script to remove periods impacted by flares. No major flares were found in the individual background light curves. The light curves were also compared ensuring no flares were missed in the shorter observations. No flare periods were identified. The observations used and their corresponding exposure times are listed in Table 1.

The earlier 90 ks observation of H1821+643 taken with ACIS-S in 2008 was severely piled up ($>$ 80 per cent) within the region of interest here. Piled-up events exceeded the upper energy cutoff and were not telemetered to the ground, which resulted in an apparent hole at the centre of the quasar PSF. This observation was focused on the surrounding galaxy cluster rather than the immediate environment of the quasar and therefore did not use a subarray (Russell et al. 2010). We did not utilize this additional data set in this study except to evaluate systematic uncertainty due to the contaminant correction. *Chandra's* ACIS instrument has decreasing soft-band effective area over time due to the deposition of a contaminant on the optical blocking filters. The rate of accumulation is varying over time and the calibration must be regularly updated (Plucinsky et al. 2018). We therefore compared the best-fitting parameters for the new and 2008 observations for identical regions at large radius to check the accuracy of the contaminant correction. We found no systematic differences.

The cluster emission extended over the full subarray so blank sky backgrounds were generated for each observation. Each background data set was reprocessed as above, reprojected to the appropriate sky position, and normalized to match the observed count rate in the 9.5$-$12 keV energy band. We note that this study focused on the luminous extended emission immediately around the quasar therefore the background subtraction was not particularly significant and the blank sky backgrounds were sufficiently well-matched to the observation.

Subpixel event repositioning was used to determine the quasar centroid for image and profile alignment across the separate observations (Li et al. 2004). For each observation, an image of the quasar was generated with a spatial resolution 10 times finer than the native resolution of 0.495 arcsec. The quasar centre was then determined with two-dimensional (2D) image fitting in SHERPA (Freeman, Doe & Siemiginowska 2001). The best-fitting centroid for each data set was used throughout to align images and position extraction regions for radial profiles and spectra. Pile-up and, to a lesser extent, the presence of extended emission will distort the PSF shape. However, this effect will be comparable for all data sets and was found to be negligible in a similar analysis of M87, which has more complex circumnuclear emission (Russell et al. 2018). Due to the subarray's limited field of view, additional point sources were only detected in a few observations taken at favourable roll angles. This limitation on the alignment, in combination with PSF asymmetries at 1 arcmin off-axis, prevented us from analysing sectors on small scales around the quasar.

3. QUASAR PSF SUBTRACTION

The quasar PSF emission dominates over the extended emission from the hot atmosphere to a radius of 4 arcsec (18 kpc) for the energy band 0.5$-$7 keV. The quasar is so bright that the PSF emission only drops below 10 per cent of the total 0.5$-$7 keV flux beyond a radius of 20 arcsec (90 kpc). The *Chandra* PSF is broader at high energies compared with low energies so the impact can be even greater in a hard energy band. The quasar PSF has a significantly harder spectrum than the thermal emission so this contribution must be carefully modelled to large radii to remove systematic increases in both normalization and measured gas temperature. It

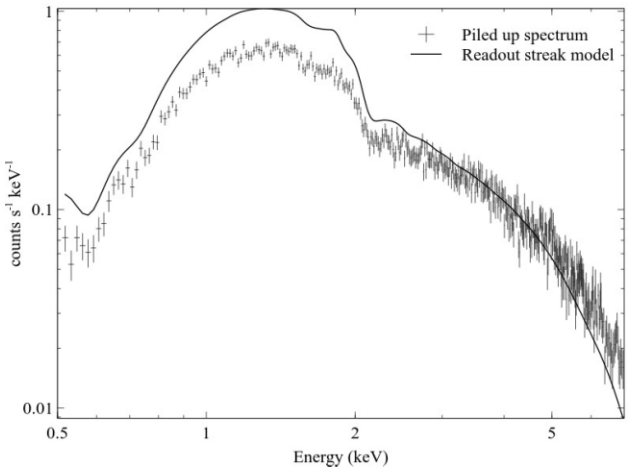

Figure 2. Quasar spectrum extracted from Obs. ID 21558 using a circular region with radius 1.5 arcsec. Approximately 25 per cent of the incident photons were piled up in the spectrum. The spectral model determined from the readout streak spectrum is shown by the solid line. This model is unaffected by pile-up. The difference between the model and the piled-up spectrum shows how pile-up hardens the observed spectrum and reduces the flux.

is not possible to cleanly spectrally separate the spatially coincident quasar and extended emission (Russell et al. 2010). Instead, we must determine the PSF contribution at each radius, fix the parameters of an appropriate spectral model that accounts for this contribution, and then fit a thermal model to the residual emission from the hot atmosphere.

A detailed model of the High Resolution Mirror Assembly (HRMA) PSF was produced before launch and calibrated with in-flight data (Jerius et al. 2000). This model is continually reviewed and updated by the CXC.[1] Given the energy dependence of the PSF, the principle input to this model is the incident quasar spectrum.

3.1 Quasar spectrum

Pile-up significantly distorts the observed spectrum of the quasar H1821+643. Fig. 2 shows the modestly piled-up spectrum extracted from a circular region centred on the quasar with a radius of 1.5 arcsec. The model illustrates the incident spectrum and demonstrates that when multiple soft photons arrived in a single frame-time these were recorded as a single hard photon. The piled-up spectrum has a significant deficit of soft photons and an excess of hard photons. The piled-up spectrum can be fitted with a statistical model of pile-up (Davis 2001) to recover the incident spectrum. However, the solutions were found to be particularly degenerate for this data set and the best-fitting result predicted a far higher level of pile-up than was consistent with the fraction of bad grades or readout streak brightness.

Other techniques to extract the incident spectrum include analysing the PSF wings (e.g. Evans et al. 2004; Hardcastle, Evans & Croston 2006; Mingo et al. 2011) and using only the best event grade to select single photon arrivals (grade 0, e.g. Miller, Bautz & McNamara 2017). However, the former suffered from degeneracies between the spectrum of the PSF wings and the extended hot atmosphere emission. The latter produces a spectrum free of pile-up distortions but cannot recover the flux of the incident spectrum because the ratio of grade 0 events to total incident photons remains unknown.

We therefore extracted the quasar's incident spectrum from the readout streak (see e.g. Russell et al. 2010). For each observation, ACIS accumulates photons over the frame-time of 0.4 s and then reads out the frame at a parallel transfer rate of 40 μs. For the 1/8 subarray, only 128 rows are read, which takes a total of 0.00512 s. Unlike an optical telescope, the typically very low count rate of X-ray sources ensures that a negligible number of photons arrive during readout and a shutter is not required. In the case of very bright point sources, such as H1821+643, photons do arrive during the CCD readout and appear distributed along the entire row, which creates a continuous streak. As the effective frame-time is then much shorter (40 μs), these photons are not piled up.

We extracted a spectrum in the energy range 0.5−7 keV from two narrow regions positioned over the readout streak on either side of the quasar. Each region was 20–30 pixels long and 6 pixels wide. Background cluster emission was subtracted by extracting spectra from closely neighbouring background regions either side of the readout streak. Appropriate responses were also generated. The exposure time of each readout streak spectrum was calculated by multiplying together the number of rows, the number of frames, and the transfer rate of 40 μs. For the observations of H1821+643, the readout streak exposure times ranged from 45.7 to 227.1 s with a total of 2.9 ks.

The readout streak spectra were fit together and separately in the X-ray spectral fitting package XSPEC (version 12.12.1; Arnaud 1996) using an absorbed power-law model. Two absorption components were used: The Galactic absorption component was fixed to the measured value from the LAB HI survey ($N_{\rm H} = 3.5 \times 10^{20}$ cm^{-2}; Kalberla et al. 2005) and the intrinsic absorption component was left free. When fit together, the best-fitting photon index $\Gamma = 2.13 \pm 0.06$, the intrinsic absorption $N_{\rm H,z} < 0.025 \times 10^{22}$ cm^{-2}, and the unabsorbed flux $F = 2.18 \pm 0.05 \times 10^{-11}$ erg cm^{-2} s^{-1} (0.5−7 keV, and $F = 1.22 \pm 0.07 \times 10^{-11}$ erg cm^{-2} s^{-1} for 2 − 10 keV). This best-fitting model is shown in Fig. 2. When fit separately, the best-fitting photon index and intrinsic absorption for each observation are consistent within their respective uncertainties. The quasar flux shows evidence for modest variability by up to a factor of 2 (Fig. 3).

Given the apparent lack of variability in the photon index and intrinsic absorption, we used an archival Low Energy Transmission Grating (LETG) observation of H1821+643 (Obs. ID 22958, PI: Kraft) that was taken in 2020 March, roughly in the middle of our ACIS program, to verify the best-fitting results. The LETG spectra were taken from the *Chandra* grating data archive and catalogue (TGCat; Huenemoerder et al. 2011) and fit with the same absorbed power-law model. The best-fitting photon index $\Gamma = 2.11^{+0.07}_{-0.06}$ is consistent with the readout streak spectrum result within the uncertainties and the intrinsic absorption is a comparable but more tightly constrained upper limit ($N_{\rm H,z} < 0.009 \times 10^{22}$ cm^{-2}). The LETG unabsorbed flux $F = 1.62^{+0.08}_{-0.16} \times 10^{-11}$ erg cm^{-2} s^{-1} for 0.5−7 keV is also consistent within the range of variability spanned by the ACIS observations. We therefore proceed with the quasar model spectrum given by the best-fitting parameters from the readout streak spectra with a jointly fit $\Gamma = 2.13 \pm 0.06$ and zero intrinsic absorption and power-law normalization determined separately for each observation.

The best-fitting photon index is significantly steeper than $\Gamma = 1.761^{+0.047}_{-0.052}$ measured with *Chandra* High Energy Grating (HEG) and Medium Energy Grating (MEG) spectra in 2002 (Fang et al. 2002). Using a readout streak spectrum, Russell et al. (2010) found

[1]See https://cxc.harvard.edu/ciao/PSFs/psf_central.html.

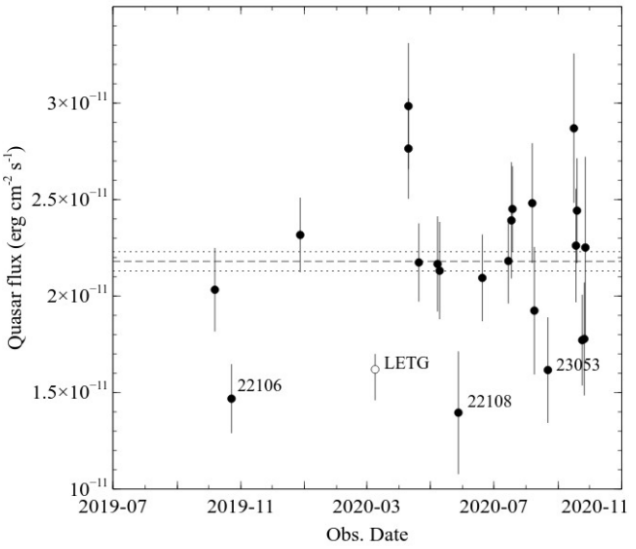

Figure 3. Unabsorbed quasar flux from the power-law component determined for each readout streak spectrum and plotted as a function of observation date. Observations with fluxes significantly different from the average are labelled. The quasar flux when fitting all observations together is shown by the dashed line with uncertainties shown by the dotted lines. The LETG data point is also shown for comparison.

a consistent Γ and measured an unabsorbed flux of $1.45^{+0.04}_{-0.03} \times 10^{-11}$ erg cm^{-2} s^{-1} for an energy range of 2−10 keV. The flux is therefore consistent with the current level of variability spanned by the new ACIS observations.

3.2 PSF simulations

The incident quasar spectral model was input to the *Chandra* Ray Tracer (Carter et al. 2003) to generate simulations of the PSF at the 1 arcmin off-axis angle. Multiple realizations were combined to ensure a full sampling of the range of optical paths in the HRMA and reduce statistical errors. MARX version 5.5.1 (Davis et al. 2012) was then used to project the simulated rays on to the ACIS-S detector and produce a simulated events file for an observation of the quasar. Pile-up effects were not included. Whilst MARX can simulate the effects of pile-up, the extended emission increases the level of pile-up in the observation and this cannot be captured by a simulation of the quasar alone. Instead, we consider the impact of mild pile-up (<5 per cent) in the 1−2 arcsec annulus on our analysis. Simulated quasar surface brightness profiles, spectra, and responses were then extracted for the same spatial regions analysed in the observation. The flux was scaled by the relative flux of each readout streak spectrum as appropriate. In this way, the quasar PSF contribution could be determined for each annulus analysed and in separate observations if needed.

Fig. 4 shows surface brightness profiles extracted from the observation and the quasar PSF simulation for the energy band 0.5−7 keV. These profiles were extracted from concentric annuli, centred on the quasar, and each 1 arcsec wide. The blank sky background was subtracted and the profiles were exposure corrected. Uncertainties from the best-fitting quasar spectral model were evaluated by running additional PSF simulations and are shown as a shaded region on the residual surface brightness profile. Fig. 4 (top panel) shows that the PSF simulation predicts a higher surface brightness than the observed profile within a radius of 1 arcsec. This is due to pile-up, which suppresses the flux of the observed profile. The bright quasar

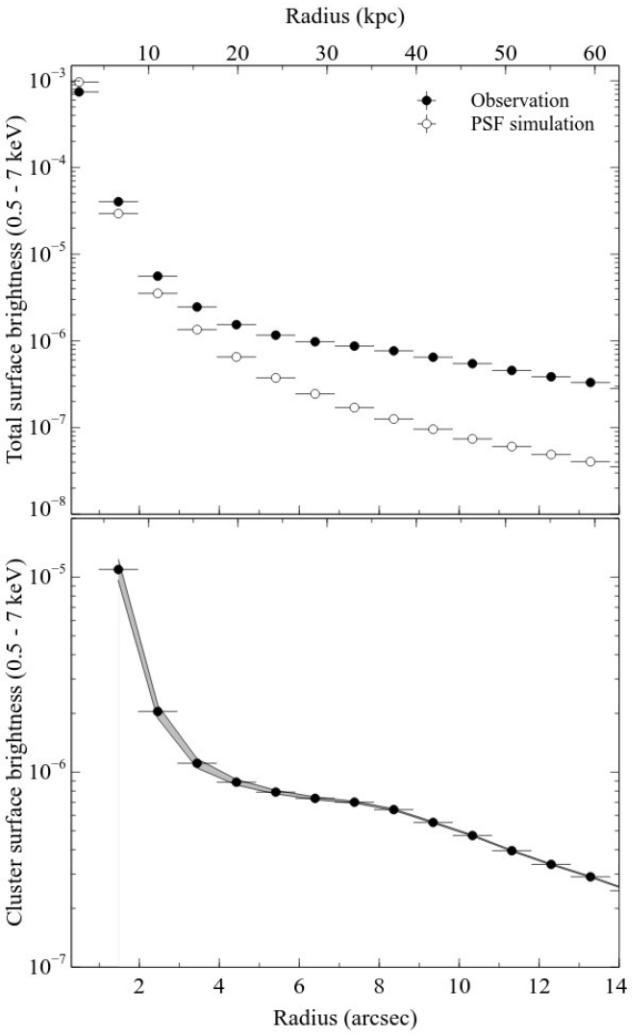

Figure 4. Top panel: Surface brightness profiles (cts cm^{-2} s^{-1} arcsec^{-2}) for the observation and the PSF simulation in the energy range 0.5−7 keV. Bottom panel: Residual surface brightness profile tracing the extended emission of the hot atmosphere (PSF simulation subtracted). Uncertainties from the best-fitting quasar spectral model are shown by the shaded band. The PSF simulation does not include pile-up, therefore the predicted PSF flux exceeds the observed flux for the 1−2 arcsec data point.

PSF clearly dominates over the hot atmosphere to a radius of 4 arcsec and then the PSF wings comprise > 10 per cent of the total flux to a radius of 20 arcsec. However, even after subtraction of the PSF, the residual profile shows a strong peak within a radius of 4 arcsec (18 kpc) suggesting that the surface brightness of the hot atmosphere increases by more than an order of magnitude. Given the spatial coincidence with the bright quasar, it is natural to assume this peak is a result of an undersubtraction of the quasar PSF. However, this would require an underestimation by ∼ 35 per cent for the energy band 0.5−7 keV (increasing > 200 per cent in a soft band).

We consider the likelihood of such a significant underestimation of the quasar PSF. Whilst this PSF subtraction technique has been utilized effectively in the presence of bright hot atmospheres in a number of previous studies (Russell et al. 2010; Siemiginowska et al. 2010; Bambic et al. 2023), the dominance of the quasar PSF in H1821+643 renders this analysis particularly challenging. There are a number of potential systematics to consider. MARX version 5 uses the ASPECTBLUR parameter to blur the PSF by the uncertainty in the

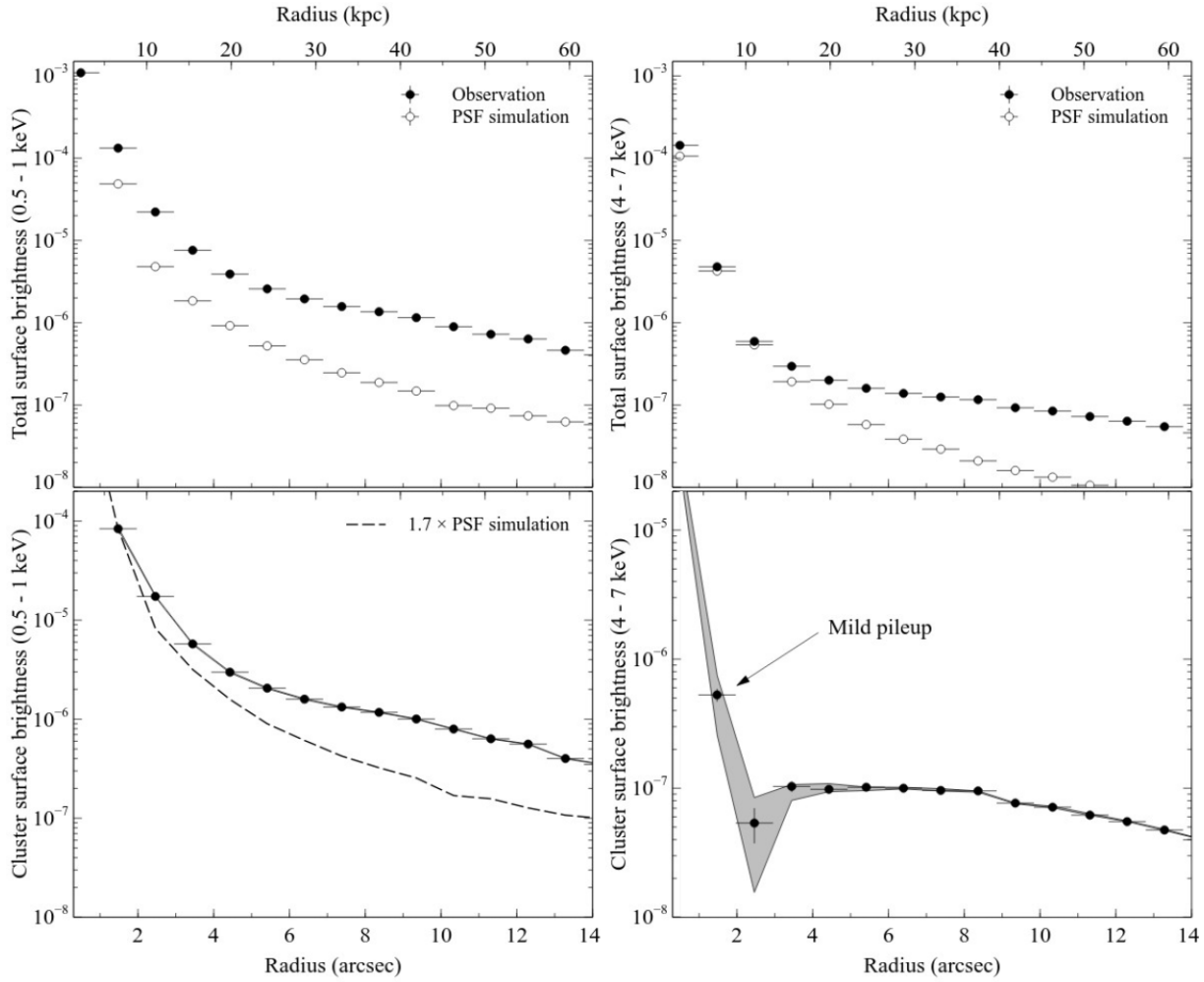

Figure 5. The soft-band surface brightness profile (0.5−1 keV) is dominated by emission from the centre of the hot atmosphere (left panel). The hard-band surface brightness profile (4−7 keV) is dominated by quasar PSF emission and the projected outer, hotter layers of the cluster atmosphere. Top panels show the observed profiles and the quasar PSF simulation. The bottom panels show the residual profiles where the PSF simulation has been subtracted. Units are cts cm^{-2} s^{-1} $arcsec^{-2}$. The hard-band profile is free of pile-up beyond 2 arcsec radius and shows no strong residuals on arcsec scales from the quasar PSF. In contrast, the soft-band profile shows a clear central spike that is broader than the PSF.

aspect solution. The observed PSF has been found to be wider than the equivalent simulated PSF so this parameter is typically empirically adjusted to match the observation of interest and is dependent on the source spectrum and the observation date. There is also evidence that the soft-band ACIS PSF (< 0.8 keV) has broadened in observations since ∼2017, likely due to the continued contaminant build-up on the ACIS filters. The presence of bright, extended emission makes it impossible to fine-tune the PSF model to mitigate these problems. Furthermore, the model accounting for the change in effective area under the contaminant build-up is continually evolving. An underestimation of the contaminant layer would artificially suppress the measured quasar flux, leading to an undersubtraction of this component and a clear excess at low energies with a similar slope to the PSF. We note however that an underestimation by ∼ 200 per cent appears highly unlikely given *Chandra's* ongoing programme of detailed calibration observations. We tested the impact of the latest contaminant model update available in CALDB version 4.10.2 and found that the measured quasar flux from the readout streak increased by 2.4 per cent for the energy range 0.5−1 keV.

The best way to determine the impact of systematic uncertainties on the PSF simulation is to examine the PSF-subtracted surface brightness profile in a hard band. Whilst the soft-band emission is often highly structured at the centres of brightest cluster galaxies, usually due to dense, cool gas filaments and rims around cavities, the hard-band emission traces the hotter, projected cluster gas, which is more uniform. Any substructure on small scales around the quasar in a hard-band surface brightness profile is therefore likely due to inaccuracies in the PSF subtraction alone.

Fig. 5 (right panel) shows the surface brightness profiles extracted from the observation and the quasar PSF simulation for the energy band 4−7 keV. We note that pile-up artificially boosts the observed flux in the hard band within a radius of 1 arcsec and this is not captured by the PSF simulation. Fig. 2 shows how pile-up distorts the spectral shape with piled-up soft-band photons detected as an excess in the hard band. This region is therefore not considered further. As discussed in Section 2, the region from 1−2 arcsec is also likely affected by a low level of pile-up. This produces the observed spike in the hard-band surface brightness profile in this region as pile-up boosts the total hard-band flux by ∼8 per cent. The flux in the 2−3 arcsec region is not artificially increased by pile-up and is therefore the best indicator of an accurate PSF subtraction. A modest drop in the hard-band flux here suggests that the PSF is marginally

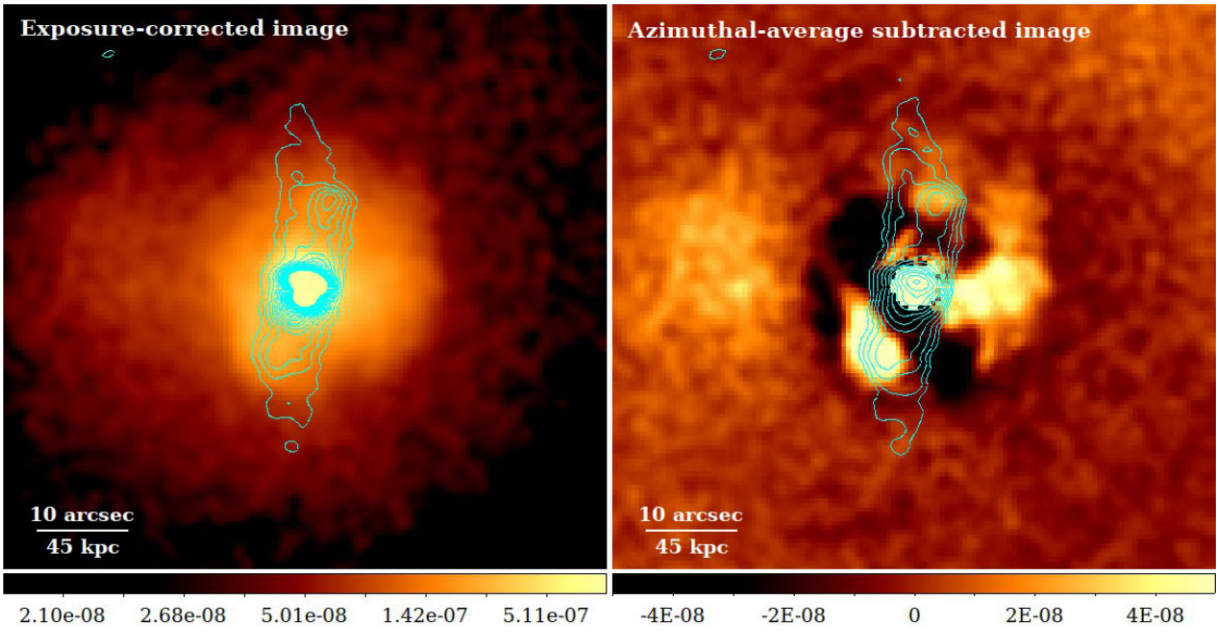

Figure 6. Merged image for the energy range 0.5−7 keV. Image is exposure corrected with units of cts cm^{-2} s^{-1} $pixel^{-1}$ and smoothed with a 2D Gaussian with $\sigma = 1.5$ arcsec. Readout streaks were excluded from each separate observation and the range in roll angle ensures that the removal is not readily visible once merged. VLA 1.4 GHz radio contours at 5σ, 10σ, 15σ... from Blundell & Rawlings (2001) are also shown. N is up and E is to the left. Right panel: Residual image where the average surface brightness at each radius, centred on the quasar, has been subtracted. Note that, whilst this method produces residuals around the quasar, the subtraction using the PSF simulation does not.

oversubtracted by the model. However, this is not significant given the uncertainties from the readout streak spectral model (shown by the grey-shaded region). Beyond the pile-up affected regions, the hard-band surface brightness profile has a smooth gradient with no significant substructure in the region dominated by the quasar PSF.

Whilst the PSF model is clearly a good match in the hard band, the ACIS PSF has broadened significantly at low energies since ∼2017 and this systematic requires a separate evaluation. Using the readout streak, which is unaffected by pile-up, we extract the surface brightness for the energy range 0.5−1 keV within a radius of 1 arcsec. The measured surface brightness matches the PSF simulations in this region within the uncertainties. Any significant broadening of the PSF (∼ 0.1 arcsec), due to the contaminant build-up or the ASPECTBLUR parameter, would reduce the measured surface brightness in this region (spreading the flux to larger radii) and produce a mismatch with the readout streak result. These effects are therefore too small to explain the extended soft-band peak.

Fig. 5 (left panel) shows the soft-band surface brightness profiles. There is a strong central peak in the residual profile, which is due to a factor of ∼30 increase in the surface brightness over a few arcsec (∼ 13 kpc). The PSF model flux would need to be increased by a factor of ∼3 to remove this peak. Such a large increase would be inconsistent with the observed level of pile-up (Section 2) and would still leave a residual soft-band peak because the quasar PSF is significantly narrower than the soft-band peak (shown by comparison with the dashed line in Fig. 5, left panel).

In summary, the soft-band surface brightness of the galaxy's hot atmosphere increases by a factor of ∼30 within the central few arcsec (∼ 13 kpc). This peak cannot be explained by an undersubtraction of the quasar PSF. The hard-band surface brightness profile shows no significant residuals on these scales (excluding regions affected by pile-up). The soft-band PSF flux would have to be underestimated by a factor of ∼3 and the profile must broadened by ∼ 0.5 arcsec to explain this peak. These are both inconsistent with the flux measured from the readout streak spectrum, which is unaffected by pile-up. The conclusion is a clear, extended soft-band peak.

Rather than an undersubtraction of the quasar emission, it is more likely that our PSF model oversubtracts emission. The strength of the extended soft-band peak indicates that the readout streak spectrum will contain a non-negligible contribution from the hot atmosphere. It was not possible to spectrally separate this from the quasar emission. Therefore, the PSF model contains a low level of soft extended emission that is then effectively subtracted from the neighbouring annuli. We consider the impact of this and mitigation in Section 5.1.

4. IMAGE ANALYSIS AND SURFACE BRIGHTNESS PROFILES

Fig. 6 shows the merged image for the new *Chandra* data set and a residual image, where the average surface brightness at each radius has been subtracted from the image. The quasar emission dominates the central few arcsec and the extended emission dominates beyond a radius of 4 arcsec. The extended cluster atmosphere is clearly asymmetrical about the quasar with bright spurs of emission along the N-S axis of the radio lobes and to the W to a radius of ∼ 15 arcsec. VLA 1.4 GHz contours from Blundell & Rawlings (2001) show that the SE spur is a bright rim around the S radio lobe and is likely associated with an X-ray surface brightness depression or cavity. The N extension similarly extends around the N radio lobe and is also coincident with an X-ray surface brightness depression. Whilst there are other depressions visible in the residual X-ray image, these appear to be a result of the azimuthal averaging with clear excess emission at the same radius. The cavities are each located 27 kpc from the nucleus and have radii of ∼ 14 kpc. The W spur appears to terminate at a surface brightness edge that runs W to S around the

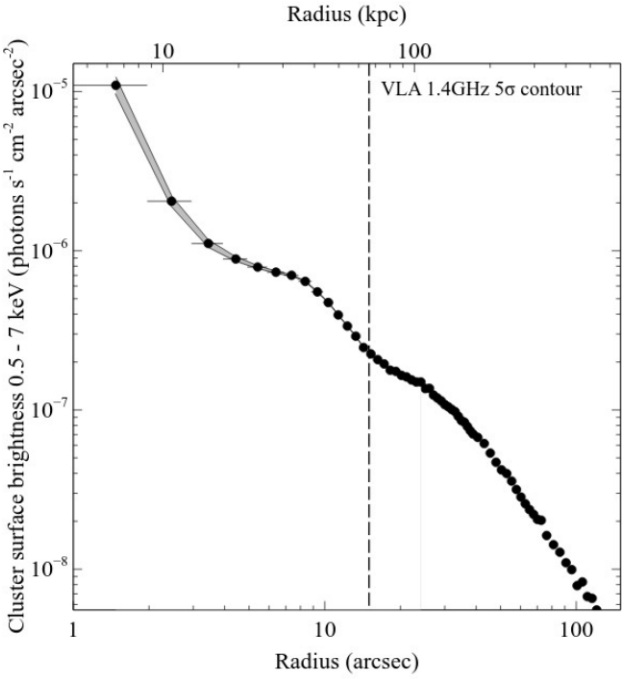

Figure 7. Residual surface brightness profile (cts cm^{-2} s^{-1} arcsec^{-2}) in the energy range 0.5−7 keV extending to large radius. The quasar PSF emission has been subtracted. The approximate extent of the radio emission to the N and S of the quasar is shown by the dashed line (see Fig. 6). Uncertainties from the best-fitting quasar spectral model are shown by the shaded band.

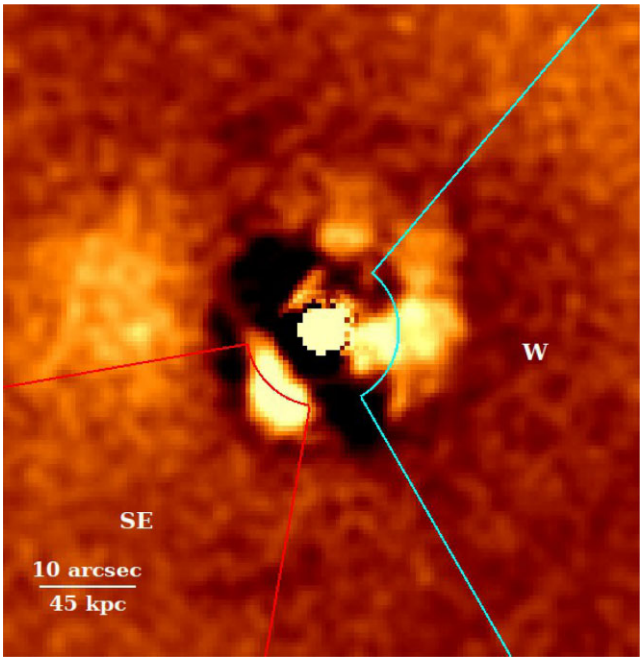

Figure 8. Residual image (see Fig. 6) with sectors overlaid that cover the surface brightness edge that runs W to S around the cluster core.

cluster core. This edge is sharpest to the NW and SE. Beyond the immediate environment of the radio lobes, the cluster emission on 100 kpc scales is asymmetric, with greater extension to the E (Fig. 6, right panel).

The strong peak in the extended emission within the central few arcsec is only readily apparent once the quasar PSF has been subtracted. Fig. 7 shows the PSF-subtracted surface brightness profile with an increase of more than an order of magnitude within a radius of 3 arcsec (13 kpc). This increase is unlikely to be due to the quasar PSF wings (see Section 3.2) or scattering of quasar emission off free electrons and dust within the host galaxy. To demonstrate the latter, we compare the ratio of the 'scattered' emission, $F_{\rm scatt}$, with the direct emission from the AGN, $F_{\rm AGN}$.

$$\frac{F_{\rm scatt}}{F_{\rm AGN}} = \frac{1}{L_{\rm AGN}} \int \left(\frac{L_{\rm AGN}}{4\pi r^2}\right) \sigma_{\rm T} n_{\rm e} {\rm d}V, \quad (1)$$

where $L_{\rm AGN}$ is the AGN luminosity and $\sigma_{\rm T}$ is the Thomson scattering cross-section. Assuming a power-law form for the electron density profile,

$$n_{\rm e} = n_{\rm e,r_{max}} \left(\frac{r}{r_{\rm max}}\right)^{-\zeta}, \quad (2)$$

we can integrate equation (1) over the radial range that covers the strong increase in observed surface brightness from $r_{\rm min} = 1$ arcsec (4.4 kpc) to $r_{\rm max} = 4$ arcsec (17.6 kpc). This produces an equation of the form

$$\frac{F_{\rm scatt}}{F_{\rm AGN}} = \sigma_{\rm T} n_{\rm e,r_{max}} \left(\frac{r_{\rm max}}{1-\zeta}\right) \left[1 - \left(\frac{r_{\rm min}}{r_{\rm max}}\right)^{1-\zeta}\right]. \quad (3)$$

For $n_{\rm e,r_{max}} \sim 0.046 \pm 0.006$ cm^{-3} and $\zeta = 3.04 \pm 0.11$ (appropriate from 1−4 arcsec radius, see Section 5.1), we predict $F_{\rm scatt}/F_{\rm AGN} = 0.013 \pm 0.002$. The observed ratio is nearly an order of magnitude higher, $F_{\rm scatt}/F_{\rm AGN} = 0.090 \pm 0.002$. Therefore, the observed increase in surface brightness is far too bright to be scattered quasar light. In Section 5.1, we show that the strong surface brightness peak is instead from thermal gas emission.

Beyond the quasar's immediate environment, the radio lobes are contained within a broad surface brightness edge at ∼15 arcsec (65 kpc). The filaments and asymmetrical structure can be seen from surface brightness profiles extracted in sectors (Fig. 8). The selected sectors demonstrate the shift in radius of the surface brightness edge from 13 arcsec (57 kpc) in the SE sector to 20 arcsec (88 kpc) in the W sector (Fig. 9).

5. SPECTRAL ANALYSIS

We mapped the cluster gas properties by extracting spectra in full annuli, sectors, and free-form regions. The latter covered pixels of similar surface brightness and were generated with a contour binning algorithm (Sanders 2006). The contribution from the quasar PSF was modelled with an absorbed power-law component. The power-law parameters were determined by fitting this model to spectra extracted in identical spatial regions in the PSF simulation. Each region selected had at least 5000 counts spread across 22 separate spectra (one from each observation). Appropriate response files were generated and background spectra were extracted from the tailored blank sky fields (Section 2). Spectra from all observations were fit simultaneously in XSPEC over the energy range 0.5−7 keV and grouped to ensure a minimum of 20 counts per spectral channel. The χ^2-statistic was used to determine the best-fitting model.

The cluster emission was modelled with an absorbed APEC model (Smith et al. 2001). The absorption of this component was fixed to the Galactic value (Section 3.1) and the redshift was fixed to $z = 0.296$. The temperature, metallicity, and normalization parameters were left free. Uncertainties from the best-fitting quasar spectral model were also assessed (Section 3.1). Statistical uncertainties in the PSF model

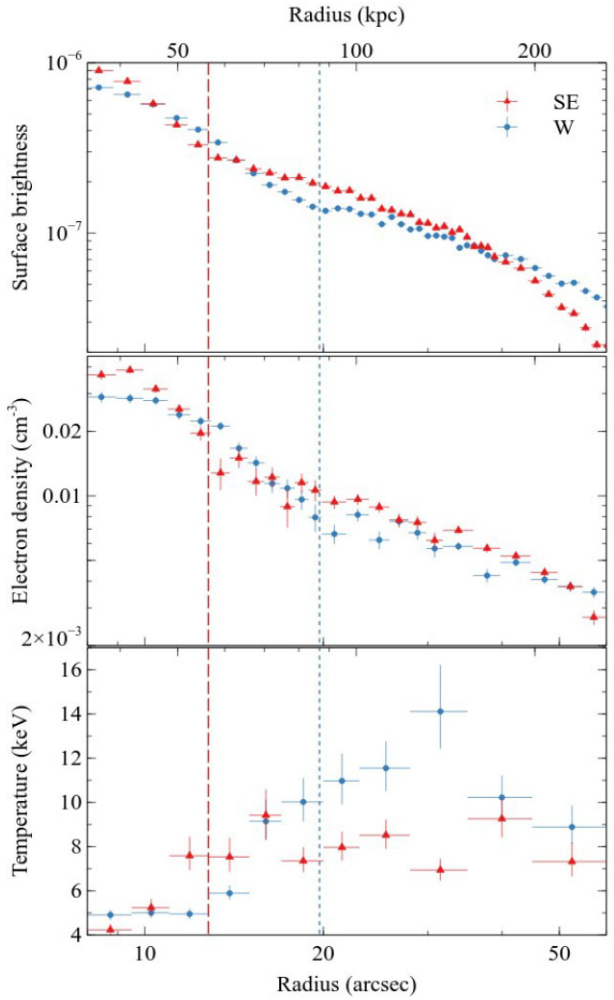

Figure 9. Upper panel: Surface brightness profiles for the SE and W sectors (see Fig. 8) with units of cts cm^{-2} s^{-1} arcsec^{-2}. Middle panel: Deprojected electron density profiles. Lower panel: Projected gas temperature profiles. Note that the profiles do not extend into the region affected by the quasar PSF. The location of surface brightness edges in the SE and W profiles are shown by the vertical lines (red dashed and blue dotted, respectively).

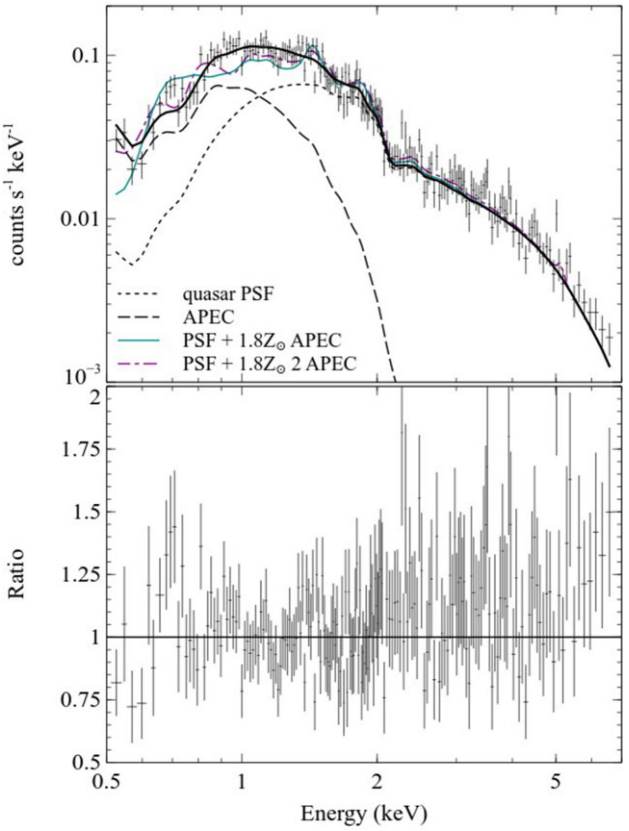

Figure 10. Upper panel: Spectrum for Obs. ID 21558 extracted from an annulus from 1 to 2 arcsec radius. The spectrum is grouped with a minimum of 20 counts per channel. The contribution from the quasar PSF wings has been determined from the PSF simulation and is shown by the dotted line. The remaining emission is likely thermal emission from the ISM and is modelled with an APEC component (dashed line). The total model is shown by the thick, solid line. The best-fit to this single spectrum gives $\chi^2 = 190$ for 180 degrees of freedom ($\chi^2_\nu = 1.06$). The total models for fixed metallicity of 1.8 Z$_\odot$ and one ($\chi^2_\nu = 1.81$) and two ($\chi^2_\nu = 1.51$) APEC components are shown by the thin, solid and dash–dotted lines, respectively. Lower panel: Ratio of the data to the best-fitting model. The strongest residuals are above 5 keV and therefore most likely due to pile-up as expected for this region (see Section 2).

parameters were found to be less than the statistical uncertainties in the cluster emission parameters at each radius.

All best-fitting parameters were determined by fitting simultaneously to spectra from the 22 separate observations. The continual reduction in effective area due to the contaminant build-up prevents us from adding spectra together. However, in Fig. 10, we show a spectrum extracted from 1−2 arcsec radius from a long individual observation with a typical PSF flux (Obs. ID 21558). This spectrum has over 7000 counts and was grouped with a minimum of 20 counts per channel for clarity. We overplot the corresponding best-fitting model and individual components to demonstrate the quality of the fit and the impact of the quasar PSF. The best-fitting parameters are all consistent with the results for the simultaneous fit to all spectra. The best-fit to the single spectrum gives $\chi^2 = 190$ for 180 degrees of freedom ($\chi^2_\nu = 1.06$). The strongest residuals are above 5 keV and therefore most likely due to pile-up (see Section 2). Modest residuals at ~ 0.7 keV are also visible but the single APEC model appears to be a reasonable fit to the soft emission.

5.1 Radial profiles

Fig. 11 shows the projected temperature, projected metallicity, and deprojected electron density profiles for the cluster gas. The deprojected electron density profile was produced using the DSDEPROJ routine, which assumes spherical symmetry to subtract the projected contribution from each successive annulus (Sanders & Fabian 2007; Russell, Sanders & Fabian 2008). Regardless of the excess hard photons due to pile-up (1−2 arcsec) or the modest oversubtraction of the quasar PSF (2−3 arcsec), the gas temperature drops precipitously to 0.4 keV for both annuli inside 3 arcsec (13 kpc). This is very close to the lower bound of the APEC model and therefore in effect is an upper limit on the gas temperature. From 3 to 4 arcsec, the gas temperature increases to 0.94 ± 0.03 keV. Then, at 4 arcsec radius (18 kpc), the temperature sharply increases by a factor of 3 to $2.72^{+0.10}_{-0.09}$ keV. Beyond this radius, the temperature increase is smoother and extends up to $9.0^{+0.7}_{-0.6}$ keV at a radius of 20 arcsec (90 kpc).

The metallicity profile at the centre of H1821+643 is similarly striking. The metallicity within 3 arcsec (13 kpc) of the quasar is essentially an upper limit of 0.04 Z$_\odot$. There is a modest increase from

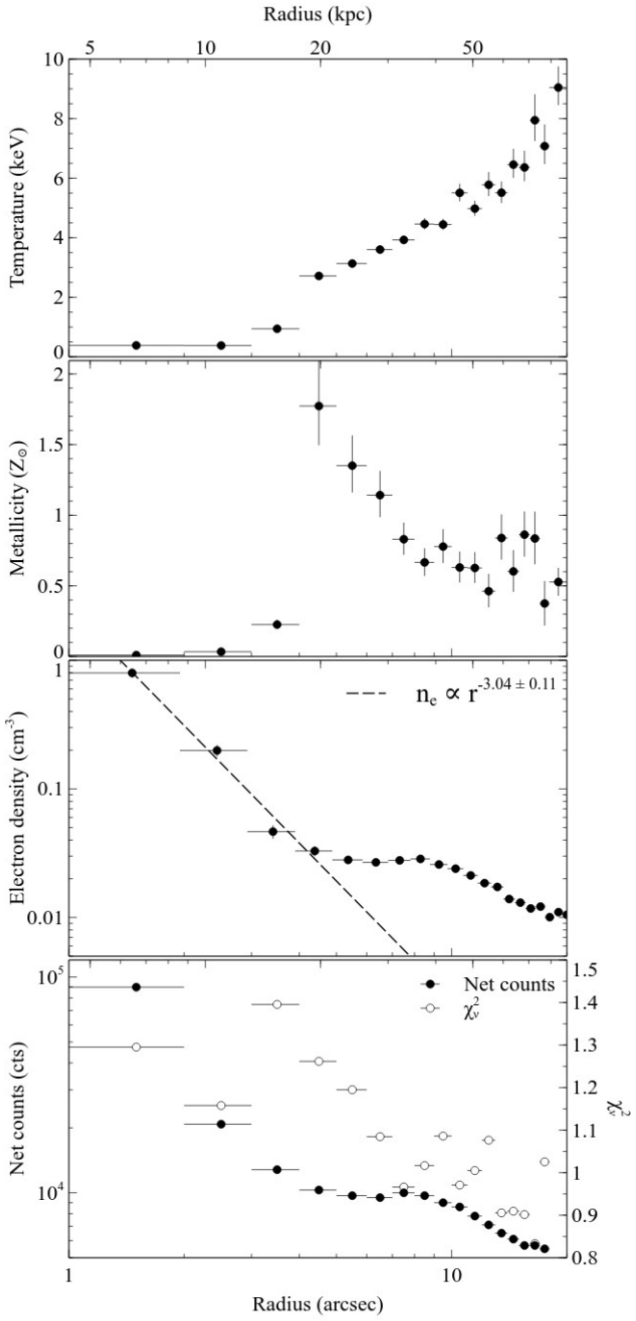

Figure 11. Upper panel: Projected temperature, projected metallicity, and deprojected electron density profiles for the cluster gas. Bottom panel: Net counts and χ^2_ν for each annulus. The quasar PSF contribution has been subtracted from each plot.

3 to 4 arcsec to an abundance of $0.23 \pm 0.03\,Z_\odot$. The metallicity then increases by a factor of roughly 10 to a peak of $1.8 \pm 0.3\ Z_\odot$ and then decreases with radius to the average value of $0.4\ Z_\odot$ at a radius approaching 100 kpc. If we fix the metallicity in the innermost radial bin to $1.8\ Z_\odot$, the corresponding best-fitting model has $\chi^2_\nu = 1.95$ ($\chi^2 = 5689$ for 2916 degrees of freedom) compared with $\chi^2_\nu = 1.30$ ($\chi^2 = 3775$ for 2915 degrees of freedom) for a free, low metallicity value. Similarly, even a modest metallicity of $0.4\,Z_\odot$ is excluded. The corresponding best-fitting model has $\chi^2_\nu = 1.73$ ($\chi^2 = 5046$ for 2916 degrees of freedom). Additional APEC or MKCFLOW components, or a free Galactic absorption component, did not significantly improve the fit or alter the low metallicity value. The only exception is for 3−4 arcsec where an additional APEC component at ~ 0.4 keV does produce a better fit with $\chi^2_\nu = 1.06$ but the metallicity remains low.

Although low metallicity would result from fitting a thermal plasma model to quasar continuum emission, we have demonstrated in Section 3.2 that our model accounts for the vast majority of the quasar emission. Another possible systematic is the low-level component of soft extended emission in the PSF model, which is then effectively oversubtracted from the surrounding annuli (see Section 3.2). For gas temperatures below $\sim$2keV, the blend of Fe L lines near 1 keV (redshifted to 0.75 keV) is particularly prominent and may be affected by this oversubtraction. We therefore repeated the spectral fitting analysis but excluded emission below 1 keV (see e.g. Ghizzardi et al. 2021). We obtain similarly tight constraints on the metallicity in the innermost two annuli and similarly low temperature values. Fig. 10 shows that these tight constraints are due to the absence of a clear Mg line at $\sim$1.1 keV (rest frame 1.4 keV) and Si and S lines at 1.5−2.3 keV (rest frame 2−3 keV). The low metallicity likely has a physical origin, which is confirmed by Suzaku observations of H1821+643 that also indicate subsolar metallicity (Reynolds et al. 2014).

The hot atmosphere within a radius of 4 arcsec (18 kpc) has likely been photoionized by the quasar emission. The ionization parameter $\xi = L/n_e r^2$ where L is the quasar luminosity above 15 eV ($1.1 \pm 0.1 \times 10^{46}$ erg s^{-1}) and n_e is the electron density at a radius of r. At a radius of 20 kpc, $\xi = 90 \pm 10$ erg cm s^{-1}. Using XSTAR, Kallman & Bautista (2001) show that, at $\xi = 90 \pm 10$ erg cm s^{-1}, Mg, O, Si, and S ions will be almost completely photoionized and Fe will be partly photoionized. If the quasar emission is beamed out of the line of sight, then we expect strong asymmetries with ions in the path of the beam completely photoionized. Russell et al. (2010) also used Cloudy simulations (Chatzikos et al. 2023) to demonstrate that the quasar emission from H1821+643 will produce a significant amount of photoionization in this region and the line emission will be suppressed. The previous *Chandra* observations could not distinguish this effect from the Fe bias created by fitting multitemperature gas with a single-temperature model. With the new data set, the dramatic decline in metallicity at small radii is revealed. This cannot be explained by Fe bias in multitemperature gas and is instead due to photoionization.

The deprojected electron density increases by a factor of $\sim$25 from a radius of 20 to 6 kpc (5 to 1.5 arcsec) at the centre of H1821+643 (Fig. 11). We fit a power-law model to this section of the density profile and find a best-fit where $n_e = 240^{+70}_{-60}\,(r/\mathrm{kpc})^{-3.04\pm0.11}$ cm^{-3}. If the gas temperature has dropped to 0.4 keV in this region, as indicated by the temperature profile, we would expect a steep rise in density as the gas is compressed by the outer atmosphere. For 0.4 keV gas in an isothermal potential with galaxy line-of-sight velocity 300 km s^{-1} (based on the total galaxy mass estimates in Fukuchi et al. 2022), the gas density in a hydrostatic atmosphere should vary as $r^{-2\mu m_H \sigma^2/k_B T}$, where the exponent is −2.9. This is consistent with the gradient of the observed density profile (Fig. 11). The observed rapid increase in gas density and decrease in temperature therefore appear consistent and suggest that the emission in this region is thermal interstellar medium (ISM).

Fig. 12 shows the radiative cooling time and free fall time profiles. The radiative cooling time,

$$t_{\rm cool} = \frac{3}{2}\frac{nk_{\rm B}T}{n_{\rm e}n_{\rm H}\Lambda\,(T,\,Z)}, \tag{4}$$

where n is the gas density, n_e is the electron density, T is the temperature, n_H is the ion density, and $\Lambda(T, Z)$ is the cooling function,

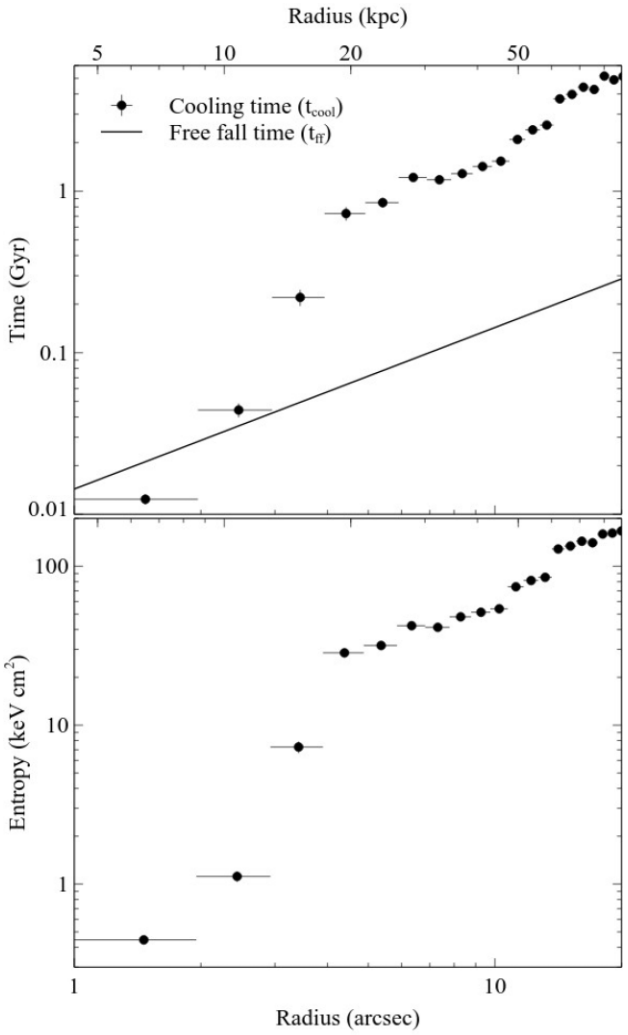

Figure 12. Upper panel: Radiative cooling time and free fall time profiles. Lower panel: Entropy profile.

which depends on the gas temperature and metallicity. If Fe is not fully photoionized within a radius of 18 kpc, the cooling function will be underestimated here by up to an order of magnitude (for 1.8 $Z_\odot$). The free fall time profile was calculated assuming an isothermal potential and $\sigma = 300$ km s^{-1} (see e.g. Hogan et al. 2017). The cooling time drops sharply below a Gyr within the central 4 arcsec (18 kpc) and falls to 12 ± 1 Myr at 1.5 arcsec (6.5 kpc). The cooling time falls below the free fall time here. The centre of H1821+643 is therefore undergoing runaway or catastrophic cooling. If the cooling function has been underestimated, the cooling time within a radius of 18 kpc is likely shorter by up to an order of magnitude and will fall below the free fall time at this larger radius.

Fig. 12 also shows the cluster entropy profile calculated from the deprojected electron density and projected temperature profiles as $K = T/n_e^{2/3}$. The innermost value drops to 0.44 ± 0.02 keV cm^2 at a radius of 6.5 kpc. This is far below the typical values for cool core clusters at similar radii of ~ 10 keV cm^2 and even below the previous record of ~ 2 keV cm^2 found at this radius in the Phoenix cluster (McDonald et al. 2019).

5.2 Contour binning maps

Beyond the quasar's immediate environment, we map the gas properties using a contour binning algorithm (Sanders 2006), which generates spatial regions by grouping together neighbouring pixels with similar surface brightness. Pixels were added until each region contained at least 1000 counts ($S/N = 32$). The quasar and its immediate environment to a radius of 4 arcsec was excluded. This region can only be analysed with full annuli because of PSF asymmetries (see Section 2). Each spectrum was fitted with an absorbed APEC model as described above. The uncertainties on the temperature value are typically 10 per cent at 3−4 keV, 20−30 per cent at 6−8 keV, and 40−50 per cent at 10−15 keV. The uncertainties on the normalization are typically 5−10 per cent. Pseudo-pressure was generated by multiplying the temperature and square root of the normalization. Whilst the metallicity was left as a free parameter, the corresponding map does not reveal significant structure beyond the radial variation shown in Fig. 11.

Fig. 13 shows the resulting temperature and pressure maps. The low-temperature gas, 3−4 keV, at the centre clearly extends along the radio jet axis, particularly along the SE edge of the S radio lobe. The temperature then increases sharply to 7−9 keV at a radius of 12 arcsec. This increase coincides with the surface brightness edge detected in the SE sector. This structure is likely to be a bright, cool rim of gas around a radio bubble (Fig. 9). The bright rim above the N radio lobe has a similarly low temperature. A further extension of cool gas is visible to the W of the quasar to a radius of $\sim$18 arcsec ($\sim$80 kpc). At this radius, the temperature then increases sharply from 4−5 keV to $>$ 10 keV. Fig. 9 shows a surface brightness edge at this radius, therefore this structure is a cold front. The temperature map also shows a hot region at $>$ 10 keV that forms an arc beyond the W cold front. Although there is no clear surface brightness edge at this radius in the W sector, the temperature increase is significant and suggests that this may be a shock-heated region. Bonafede et al. (2014) proposed that H1821+643 has undergone an off-axis or minor merger because it hosts a giant radio halo. Based on optical imaging, Hutchings & Neff (1991) suggested H1821+643 was in the late stages of a mild tidal event or merger. The W cold front, which appears unrelated to the radio lobes, the E extension of the cluster emission on large scales and the shock-heated region to the W are consistent with this picture.

6. DISCUSSION

We have presented a new 582 ks short frame-time *Chandra* observation of the quasar H1821+643, which lies at the centre of a strong cool core cluster. By carefully modelling the quasar PSF, we show that the surface brightness of the central galaxy's hot atmosphere increases by a factor of $\sim$30 within the central few arcsec ($\sim$13 kpc) and the gas temperature drops rapidly to $<$ 0.4 keV. The radiative cooling time of the gas is only 12 ± 1 Myr at a radius of 6.5 kpc and falls below the free fall time. We have demonstrated that this clear transition in the gas properties cannot be due to an undersubtraction of the quasar PSF or scattered quasar light and is instead consistent with runaway cooling of the galaxy's hot atmosphere.

6.1 Runaway cooling of the hot atmosphere

The multiwavelength data for H1821+643 are also consistent with rapid cooling of the hot gas. With a total infrared (IR) luminosity of $L_{IR,tot} = 4.6 \times 10^{46}$ erg s^{-1} $= 1.1 \times 10^{13}$ $L_\odot$ (Ichikawa et al. 2019), the central galaxy is categorized as a hyperluminous IR

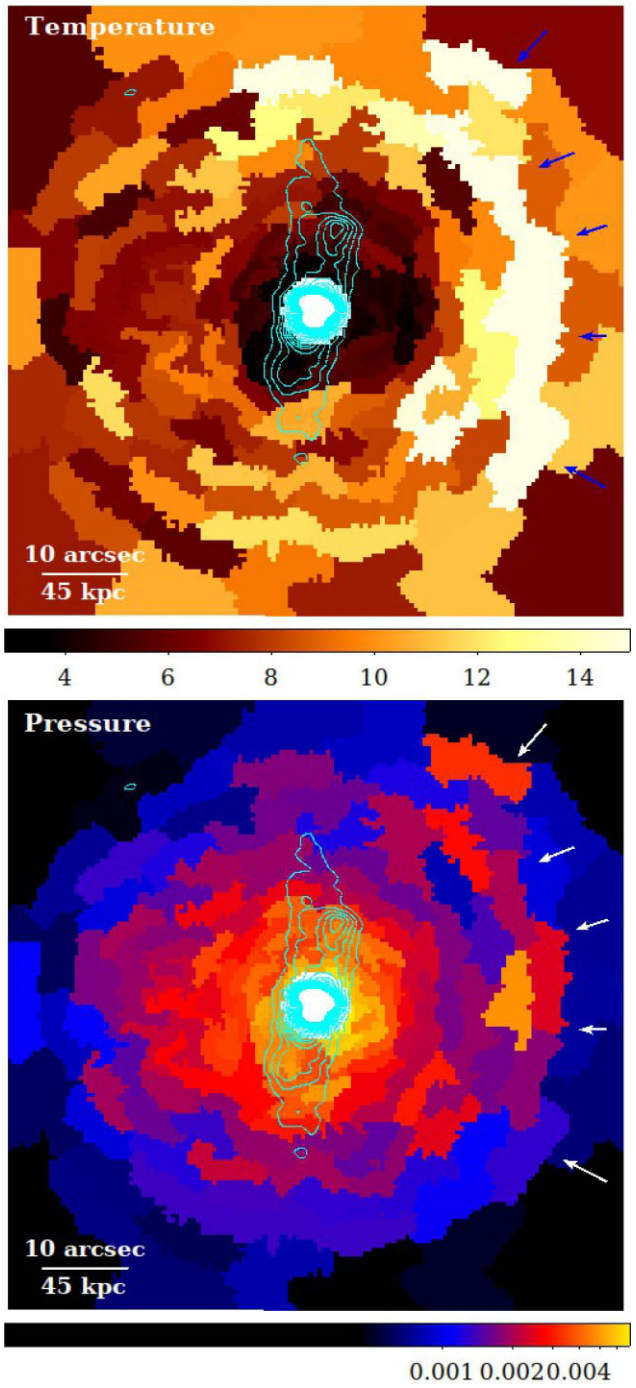

Figure 13. Upper panel: Projected temperature map (keV). Lower panel: Pseudo-pressure map (keV cm$^{-5/2}$ arcsec^{-2}). The quasar and its immediate environment to a radius of 4 arcsec have been excluded (central white circle). The radio contours from Fig. 6 are shown overlaid and a hot, relatively high pressure region to the W and NW is marked by the arrows.

galaxy. H1821+643 is likely in a strong starburst phase with an estimated star-formation rate of 120^{+120}_{-60} M$_\odot$ yr^{-1} from *Hubble Space Telescope (HST)* [O II] maps with the quasar emission subtracted (Calzadilla et al. 2022). Alternative estimates from polycyclic aromatic hydrocarbon 7.7 μm emissions (Ruiz et al. 2013) and spectral energy distribution (SED) fitting studies (Farrah et al. 2002; Fukuchi et al. 2022) confirm a high rate of star formation. This places H1821+643 amongst the most strongly star-forming brightest cluster galaxies, which include Abell 1835, IRAS 09104+4109, and MACS 1931.8+2634. Only the Phoenix cluster, at 600^{+300}_{-200} M$_\odot$ yr^{-1}, exceeds this group (McDonald et al. 2012; Calzadilla et al. 2022).

CARMA observations detect strong CO(1-0) emission from $(8.0 \pm 1.7) \times 10^9$ M$_\odot$ of molecular gas extending up to ∼4 arcsec (18 kpc) to the SE of the quasar (Aravena et al. 2011; assuming an $X_{\rm CO}$ factor that is typical of local luminous IR galaxies). Although it was not possible to resolve asymmetries in the hot gas emission on these scales, we note that the molecular gas aligns with the SE radio lobe and extension of cool X-ray gas around the bubble rim. This is indicative of stimulated cooling where the radio bubbles promote gas cooling by lifting low-entropy gas (McNamara et al. 2016). Given uncertainties in the CO-to-H_2 conversion factor and CO emission line ratios, the molecular gas mass in H1821+643 is comparable with the most gas-rich central galaxies, including the Phoenix cluster ($2.1 \pm 0.3 \times 10^{10}$ M$_\odot$; Russell et al. 2017) and A1835 ($9.9 \pm 0.5 \times 10^9$ M$_\odot$ updated for a LIRG $X_{\rm CO}$ factor; McNamara et al. 2014).

Optical and near-IR observations of the central galaxy are strongly impacted by the quasar emission but appear to support this picture. Floyd et al. (2004) analyse *HST* WFPC2 observations of H1821+643 using the F791W filter, which covers the bright Hα emission line (see e.g. long slit spectrum from Kolman et al. 1993). Floyd et al. (2004) detect a bright structure extending 4 arcsec to the SE of the nucleus. Although they note that this may be a PSF artefact, the spatial coincidence with the molecular gas emission suggests this may instead be ionized gas emission from the surface layers of a cool gas nebula. Herschel/PACS observations of H1821+643 found extended [O I] emission (tens of kpc across), which is also likely from cool gas (Fernandez-Ontiveros et al. 2016).

For runaway cooling, the gas flows steadily inwards as it cools, thereby maintaining pressure support of the overlying layers (e.g. Fabian & Nulsen 1977; Nulsen 1986). Assuming a steady-state, spherical inflow of gas, we can use the gas density and temperature profiles at the centre of H1821+643 to determine the radial flow speed and mass inflow rate. In terms of entropy, S, the energy equation for this gas flow is

$$\rho T v_{\rm r} \left(\frac{{\rm d}S}{{\rm d}r}\right) = n_{\rm e} n_{\rm H} \Lambda, \tag{5}$$

where ρ is the gas density, T is the gas temperature, $v_{\rm r}$ is the inflow speed, and $n_{\rm e} n_{\rm H} \Lambda$ is the energy radiated. We can rewrite this expression in terms of gas cooling time, $t_{\rm cool}$, and cluster entropy $K = k_{\rm B} T / n_{\rm e}^{2/3}$ (e.g. Voit 2005) as

$$v_{\rm r} \left(\frac{{\rm d}\ln K}{{\rm d}\ln r}\right) = \frac{r}{t_{\rm cool}}. \tag{6}$$

At a radius of ∼8 kpc, where $t_{\rm cool} \sim t_{\rm ff}$, the entropy gradient ${\rm d}\ln K / {\rm d}\ln r = 1.8 \pm 0.2$ and the cooling time $t_{\rm cool} = 12 \pm 1$ Myr. The inflow velocity is then 360 ± 50 km s^{-1}. This is roughly equal to the sound speed of 320 ± 20 km s^{-1} for gas at 0.4 keV. The sonic radius is therefore resolved in H1821+643, assuming that the flow is steady and spherical. As discussed in Section 5.1, if Fe is only partially photoionized within a radius of 18 kpc, the cooling function, λ, will be underestimated by up to an order of magnitude and the cooling time will be up to an order of magnitude shorter. The inflow velocity and sonic radius are therefore effectively lower limits.

Mass conservation for the gas inflow is given by

$$\dot{m}_{\rm inflow} = 4\pi\rho v_{\rm r} r^2. \quad (7)$$

The spherical mass inflow rate at a radius of 8 kpc is then $3500 \pm 500\,{\rm M}_\odot\,{\rm yr}^{-1}$. In addition to systematic uncertainties from the metallicity and the PSF model (Sections 5.1 and 3.2, respectively), the gas flow is unlikely to be completely steady and spherical given the interactions with the radio lobes. The mass inflow rate is also dependent on the cooling function. We therefore compare the mass inflow rate with the classical mass deposition rate, which instead relies on conservation of energy and may be more appropriate. The classical mass deposition rate

$$\dot{M} = \frac{2}{5}\frac{\mu m_{\rm H} L\,(r < r_{\rm cool})}{k_{\rm B} T\,(r_{\rm cool})}, \quad (8)$$

where $r_{\rm cool}$ is the cooling radius, $L(r < r_{\rm cool})$ is the gas luminosity within $r_{\rm cool}$, and $T(r_{\rm cool})$ is the gas temperature at $r_{\rm cool}$. For $r_{\rm cool} =$ 20 kpc, $\dot{M} = 3700 \pm 200\,{\rm M}_\odot\,{\rm yr}^{-1}$. This is consistent with the mass inflow rate and suggests only a modest underestimation of the cooling function.

Both calculations of the mass flow rate are overestimates because they discount the contribution of the gravitational potential energy to the power radiated. We therefore treat these values as order of magnitude estimates. Nevertheless, the mass flow rate can easily supply the observed star-formation rate of $120^{+120}_{-60}\ {\rm M}_\odot\,{\rm yr}^{-1}$ in H1821+643 and the required accretion rate on to the SMBH of $\sim$40 $\rm M_\odot\,yr^{-1}$ (Russell et al. 2010).

Deep *Suzaku* observations are consistent with this result. Reynolds et al. (2014) study the quasar spectrum with *Suzaku* and find a soft excess and significantly subsolar abundances, which they suggest is due to a Compton-induced cooling flow. Unfortunately, the very low metallicity and quasar variability preclude any meaningful constraint on the gas cooling rate from archival *XMM–Newton* Reflection Grating Spectrometer (RGS) observations.

6.2 Comparison with other strong cool core clusters

Fig. 14 shows the cluster entropy and mass flow rate profiles for H1821+643 compared with other strong cool core clusters. The entropy profile from Russell et al. (2010; see also Walker et al. 2014) covers the radial range 15−600 kpc and was used to extend the entropy profile from this analysis beyond 100 kpc. We compare the entropy profiles with the baseline entropy profile, $K \propto r^{1.1}$ from Voit (2005). The baseline profile is predicted from numerical simulations of structure formation that include only gravitational processes (no feedback). The entropy profiles for the vast majority of cool core clusters tend to this baseline at large radii and then diverge to a shallower gradient or plateau within the central $\sim$100 kpc where feedback increasingly dominates (e.g. Donahue et al. 2006; Cavagnolo et al. 2009). Using the previous *Chandra* analysis of H1821+643, which covered the radial range 15−600 kpc, Walker et al. (2014) showed that the entropy profile for H1821+643 falls significantly below this baseline on small scales and concluded that significant cooling had occurred. With an entropy profile that now extends to the central few kpc, we reveal that the entropy drops by nearly two orders of magnitude within the central 20 kpc and even falls below the previous record of 2 keV cm^2 from the other known exception, the Phoenix cluster.

Fig. 14 shows the mass flow rate as a function of radius, where the entropy profile was fitted with a broken power-law model (Babyk et al. 2018). At small radii, the vast majority of cool core clusters show strong suppression of the mass flow rate by over an order of magnitude as a result of AGN feedback (for example A2597, PKS0745, and A1835). The massive Phoenix cluster shows a weak suppression at small radii by a factor of $\sim$5, which indicates strong cooling and an underpowered AGN (McDonald et al. 2019). In contrast, the mass deposition rate in H1821+643 increases rapidly to $> 1000\,{\rm M}_\odot\,{\rm yr}^{-1}$ within 20 kpc and the minimum of $35 \pm 5\,{\rm M}_\odot\,{\rm yr}^{-1}$ occurs at larger radii, coincident with the cavities from 15−33 kpc. AGN feedback appears to be heating the hot atmosphere on tens of kpc scales in H1821+643 but cannot permeate the rapidly cooling region inside $\sim$10 kpc.

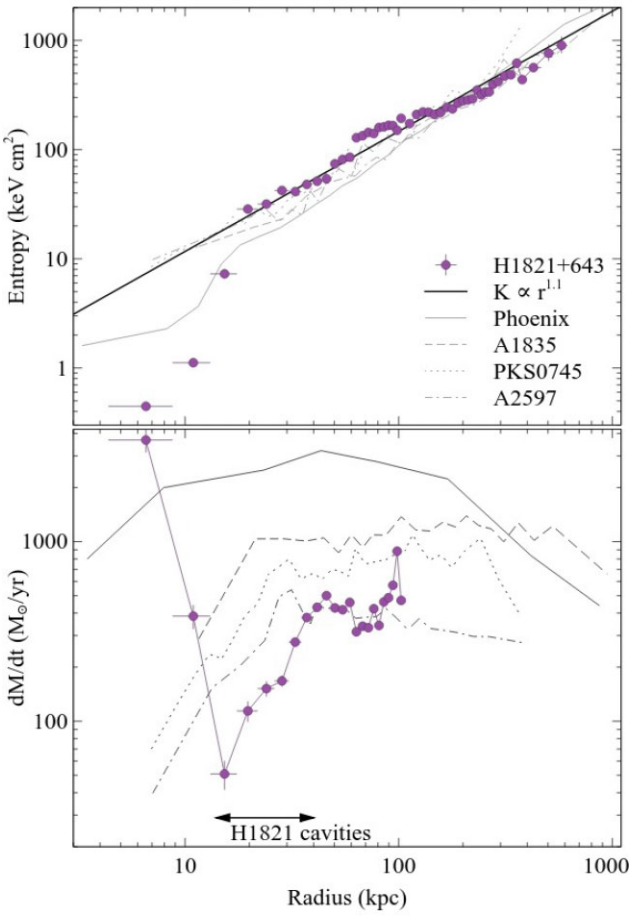

Figure 14. Upper panel: Cluster entropy profiles for H1821+643 and example strong cool core clusters A2597, PKS0745, A1835, and Phoenix. The baseline entropy profile from Voit (2005) is shown for comparison. The entropy profile from the previous *Chandra* observation of H1821+643 covers the radial range 15−600 kpc and is used to extend the profile beyond a radius of 100 kpc (Russell et al. 2010; Walker et al. 2014). Lower panel: Mass flow rate as a function of radius, where the entropy profile for each target was fit with a broken power-law model.

6.3 Runaway cooling beyond the capabilities of Compton cooling

Runaway cooling in H1821+643 extends to much larger radii than can be explained by Compton cooling by the quasar radiation. Much of the quasar power is radiated in the ultraviolet (UV). If Compton scattering between UV photons and hot electrons dominates over bremsstrahlung cooling at the galaxy centre, this will rapidly cool the hot atmosphere to the Compton temperature $T_{\rm Compton} \sim 0.4$ keV for H1821+643 (Fabian & Crawford 1990; Russell et al. 2010). The

Compton cooling time-scale, $t_{\rm Compton}$, is given by

$$t_{\rm Compton} = \frac{3n}{8n_{\rm e}} \frac{m_{\rm e}c^2}{\sigma_{\rm T} F}, \quad (9)$$

where n is the total particle density, $n_{\rm e}$ is the electron density, $m_{\rm e}$ is the electron mass, c is the speed of light, $\sigma_{\rm T}$ is the Thomson scattering cross-section, and F is the quasar flux. For Compton cooling to be significant, the Compton cooling time-scale must be shorter than the thermal bremsstrahlung radiative cooling time-scale,

$$t_{\rm Compton} < t_{\rm cool}. \quad (10)$$

Combining equations (9) and (10) gives a lower limit on the required quasar flux,

$$F > \frac{3n}{8n_{\rm e}} \frac{m_{\rm e}c^2}{\sigma_{\rm T} t_{\rm cool}}. \quad (11)$$

By multiplying by $4\pi r^2$, this can be expressed as a lower limit on the quasar luminosity,

$$L > \frac{3n}{8n_{\rm e}} \frac{m_{\rm e}c^2}{\sigma_{\rm T} t_{\rm cool}} 4\pi r^2 \quad (12)$$

where r is the distance from the quasar. Or equivalently

$$L > 3 \times 10^{45} \left(\frac{r}{\rm kpc}\right)^2 \left(\frac{t_{\rm cool}}{\rm Gyr}\right)^{-1} {\rm erg\ s^{-1}}. \quad (13)$$

For $r = 10$ kpc and $t_{\rm cool} = 50$ Myr (Fig. 12), the minimum quasar luminosity required to cool this large region is $\sim 6 \times 10^{48}$ erg s^{-1}. This is an order of magnitude greater than the measured quasar bolometric luminosity of 3×10^{47} erg s^{-1} (Fukuchi et al. 2022) and rivals the most luminous quasars known (e.g. Onken et al. 2020; Schindler et al. 2021).

The quasar may have previously been this luminous but this would be difficult to sustain. The minimum time required for a significant change in $k_{\rm B}T - k_{\rm B}T_{\rm Compton}$ is $t_{\rm Compton}$, where T is the temperature of the hot atmosphere. The total energy that must be radiated by the quasar to cause this significant change in the gas temperature is then

$$Lt_{\rm Compton} > \frac{3n}{8n_{\rm e}} \frac{m_{\rm e}c^2}{\sigma_{\rm T}} 4\pi r^2. \quad (14)$$

For $r = 10$ kpc, $Lt_{\rm Compton} > 10^{64}$ erg. For an accretion efficiency of 10 per cent, the SMBH would then have to accrete 6×10^{10} M$_\odot$ in < 100 Myr. The resulting black hole mass is close to the limit for luminous accretion given the measured spin (King 2016; Sisk-Reynés et al. 2022) and appears implausible. The estimated SMBH mass for H1821+643 is over an order of magnitude lower at $3.9^{+3.9}_{-2.0} \times 10^9$ M$_\odot$ and was determined from the broad Hβ emission line and virial, 'single-epoch' prescriptions (Koss et al. 2017). The Eddington luminosity of this SMBH is an order of magnitude below the minimum quasar luminosity required to cool the hot atmosphere to a radius of 10 kpc. Whilst Compton cooling likely enhances cooling on kpc scales, this mechanism cannot account for rapid gas cooling to a radius of 10 kpc.

6.4 An underpowered AGN?

Instead of an enhanced cooling explanation, the AGN appears to be underheating the core. In Section 4, we identify two cavities to the SE and N of the nucleus that are spatially coincident with radio lobes at 1.4 GHz. Assuming spherical cavities and using the measured thermal pressure of $\sim 3.1 \pm 0.2 \times 10^{-10}$ erg cm^{-3} at a radius of 27 kpc, we estimate that the energy required to inflate each cavity $E_{\rm cav} = 4pV = \sim 3 \times 10^{59}$erg. Using the sound speed time-scale of 27 ± 2 Myr, the total cavity power $P_{\rm cav} = 7 \times 10^{44}$ erg s^{-1}. The uncertainties on the cavity power are dominated by the cavity volume, including the unknown extent along the line of sight. We estimate uncertainties of at least a factor of 2 in the cavity power.

The cavity power appears low compared with cooling losses of $2.44 \pm 0.08 \times 10^{45}$ erg s^{-1} within a radius of 20 kpc and a total of $\sim 3.5 \times 10^{45}$ erg s^{-1} within the cooling radius of 90 kpc (the radius at which the cooling time is 7.7 Gyr or the time since $z = 1$). The cavity power appears insufficient to balance radiative losses by a factor of $\sim$5. Furthermore, Fig. 14 suggests that the cavity power is dissipated on scales of tens of kpc and has limited impact on the rapidly cooling region within a radius of 10 kpc.

High-velocity quasar winds could provide additional mechanical feedback. However, no obvious evidence for X-ray absorbing winds was found in *Chandra* HETG and LETG spectra from 2001 or in FUSE spectra from 1999 (Oegerle et al. 2000; Fang et al. 2002; Mathur, Weinberg & Chen 2003). Outflows could be oriented in the plane of the sky and not evident along our line of sight. Whilst strong and broad absorption signatures from winds can be detected in CCD spectra, the variable quasar continuum emission and evolving contaminant correction made it very difficult to detect additional absorption above the Galactic column density.

McDonald et al. (2018) suggest that the central SMBHs in the most massive galaxy clusters will be undersized compared with the mass of the cool core (see also Calzadilla et al. 2022). This naturally results from a merger scenario, where low entropy gas from the smaller halo sinks to the centre of the larger halo much faster than dynamical friction can merge the central galaxies. This may explain the weak suppression of the cooling flow at the centre of the Phoenix cluster (McDonald et al. 2019; total cluster mass $\sim 2 \sim 10^{15}$ M$_\odot$). With a total mass of $0.6-1 \times 10^{15}$ M$_\odot$ (Planck Collaboration VIII 2011; Walker et al. 2014), the galaxy cluster hosting H1821+643 is also a particularly massive system and the large-scale X-ray, optical and radio structure implies a recent merger (see Section 5.2). However, whilst the AGN is underheating, it is not clear that this is the result of an undersized SMBH. For SMBH accretion close to the Eddington rate, cavity power reaches an observed maximum of $\sim 10^{-2} L_{\rm Edd}$ (Russell et al. 2013). For H1821+643, the maximum cavity power should then be $\sim 5 \times 10^{45}$ erg s^{-1}, or roughly an order of magnitude higher than is observed, and comparable with the cooling luminosity. AGN feedback in H1821+643 may simply be undergoing a period of underheating.

7. CONCLUSIONS

Using a deep, short frame-time *Chandra* observation and a detailed PSF simulation, we extracted the properties of the hot atmosphere within 20 kpc of the low-redshift quasar H1821+643. The soft-band surface brightness increases sharply by a factor of $\sim$30 within the central 10 kpc. This cannot be explained by an undersubtraction of the quasar PSF or scattered quasar light. The hard-band surface brightness profile, which is dominated by the quasar emission, shows no significant residuals on the arcsec scales of the PSF. The observed level of pile-up is inconsistent with an underestimation of the soft-band PSF flux by the required factor of >3 and the soft-band excess is significantly extended compared with the PSF. The gas properties in the soft-band peak are instead consistent with thermal ISM emission. The gas temperature drops sharply from 2 keV at a radius of 20 kpc to < 0.4 keV at 10 kpc. The gas density rises rapidly by more than an order of magnitude over this radial range

with a gradient that is consistent with hydrostatic compression of the hot atmosphere. The metallicity is particularly low here and, based on the ionization parameter, the gas has likely been photoionized by the quasar emission. We show that the sharp increase in gas density and decrease in temperature are consistent and conclude that the soft-band peak is due to thermal ISM emission. The radiative cooling time of the gas is only 12 ± 1 Myr at a radius of 6.5 kpc and falls below the free fall time. The hot atmosphere at the centre of H1821+643 has therefore formed a cooling flow. Under the assumptions of a steady and spherical gas flow, we resolve the sonic radius.

The measured mass deposition rate of up to 3000 $M_\odot\,yr^{-1}$ can easily supply the high star-formation rate of 120^{+120}_{-60} $M_\odot\,yr^{-1}$ in H1821+643 and the required accretion rate on to the quasar of $\sim$40 $M_\odot\,yr^{-1}$. Multiwavelength observations of the massive molecular gas reservoir and extensive nebula of ionized gas support the interpretation of a cooling flow. Whilst it is likely that Compton cooling by the quasar radiation enhances gas cooling on kpc scales, the quasar luminosity is at least an order of magnitude too faint to cool the entire 20 kpc region of the cooling flow. Instead, the AGN appears to be underheating the cluster core by a factor of $\sim$5. Furthermore, the energy input by the cavities appears to suppress gas cooling on tens of kpc scales but has limited impact within the rapidly cooling region within 10 kpc. It is possible that the SMBH is undersized, likely due to a recent merger, but it may alternatively be undergoing a period of underheating.

ACKNOWLEDGEMENTS

We thank the reviewer for helpful comments that improved the paper. HRR acknowledges support from an STFC Ernest Rutherford Fellowship and an Anne McLaren Fellowship from the University of Nottingham. PEJN was supported under NASA contract NAS8-03060. TEB is supported by the Doctoral Training Centre in AI at the University of Nottingham. WNB acknowledges support from *Chandra* X-ray Center grant AR1-22006X and the Penn State Eberly Endowment. LC is supported by an STFC studentship. This research has made use of data from the *Chandra* X-ray Observatory and software provided by the *Chandra* X-ray Center (CXC). Support for this work was provided by the National Aeronautics and Space Administration through *Chandra* Award Number G09-20119X issued by the *Chandra* X-ray Center, which is operated by the Smithsonian Astrophysical Observatory for and on behalf of the National Aeronautics Space Administration under contract NAS8-03060. This work used observations obtained with *XMM–Newton*, an ESA science mission funded by ESA Member States and USA (NASA). Many of the plots in this paper were made using the VEUSZ software, written by Jeremy Sanders. This research made use of ASTROPY, a community-developed core Python package for Astronomy (Astropy Collaboration et al. 2022).

DATA AVAILABILITY

The *Chandra* data described in this work are available in the *Chandra* data archive (https://cxc.harvard.edu/cda/). Processed data products detailed in this paper will be made available on reasonable request to the author.

REFERENCES

Aravena M., Wagg J., Papadopoulos P. P., Feain I. J., 2011, ApJ, 737, 64
Arnaud K. A., 1996, in Jacoby G. H., Barnes J., eds, ASP Conf. Ser. Vol. 101, Astronomical Data Analysis Software and Systems V. Astron. Soc. Pac., San Francisco, p. 17
Astropy Collaboration et al., 2022, ApJ, 935, 167
Babyk I. V., McNamara B. R., Nulsen P. E. J., Russell H. R., Vantyghem A. N., Hogan M. T., Pulido F. A., 2018, ApJ, 862, 39
Bambic C. J., Russell H. R., Reynolds C. S., Fabian A. C., McNamara B. R., Nulsen P. E. J., 2023, MNRAS, 522, 4374
Blundell K. M., Rawlings S., 2001, ApJ, 562, L5
Bonafede A. et al., 2014, MNRAS, 444, L44
Bower R. G., Benson A. J., Malbon R., Helly J. C., Frenk C. S., Baugh C. M., Cole S., Lacey C. G., 2006, MNRAS, 370, 645
Calzadilla M. S. et al., 2022, ApJ, 940, 140
Carter C., Karovska M., Jerius D., Glotfelty K., Beikman S., 2003, in Payne H. E., Jedrzejewski R. I., Hook R. N., eds, ASP Conf. Ser. Vol. 295, Astronomical Data Analysis Software and Systems XII. Astron. Soc. Pac., San Francisco, p. 477
Cavagnolo K. W., Donahue M., Voit G. M., Sun M., 2009, ApJS, 182, 12
Chatzikos M. et al., 2023, Rev. Mex. Astron. Astrofis., 59, 327
Churazov E., Sunyaev R., Forman W., Böhringer H., 2002, MNRAS, 332, 729
Croton D. J. et al., 2006, MNRAS, 365, 11
Davis J. E., 2001, ApJ, 562, 575
Davis J. E. et al., 2012, in Takahashi T., Murray S. S., den Herder J.-W. A., eds, Proc. SPIE Conf. Ser. Vol. 8443, Space Telescopes and Instrumentation 2012: Ultraviolet to Gamma Ray. SPIE, Bellingham, p. 84431A
Di Matteo T., Springel V., Hernquist L., 2005, Nature, 433, 604
Donahue M., Horner D. J., Cavagnolo K. W., Voit G. M., 2006, ApJ, 643, 730
Evans D. A., Kraft R. P., Worrall D. M., Hardcastle M. J., Jones C., Forman W. R., Murray S. S., 2004, ApJ, 612, 786
Fabian A. C., 1994, ARA&A, 32, 277
Fabian A. C., 2012, ARA&A, 50, 455
Fabian A. C., Crawford C. S., 1990, MNRAS, 247, 439
Fabian A. C., Nulsen P. E. J., 1977, MNRAS, 180, 479
Fabian A. C. et al., 2000, MNRAS, 318, L65
Fabian A. C., Sanders J. S., Taylor G. B., Allen S. W., Crawford C. S., Johnstone R. M., Iwasawa K., 2006, MNRAS, 366, 417
Fang T., Davis D. S., Lee J. C., Marshall H. L., Bryan G. L., Canizares C. R., 2002, ApJ, 565, 86
Farrah D., Serjeant S., Efstathiou A., Rowan-Robinson M., Verma A., 2002, MNRAS, 335, 1163
Fernandez-Ontiveros J. A., Spinoglio L., Pereira-Santaella M., Malkan M. A., Andreani P., Dasyra K. M., 2016, ApJS, 226, 19
Floyd D. J. E., Kukula M. J., Dunlop J. S., McLure R. J., Miller L., Percival W. J., Baum S. A., O'Dea C. P., 2004, MNRAS, 355, 196
Freeman P., Doe S., Siemiginowska A., 2001, in Starck J.-L., Murtagh F. D., eds, Proc. SPIE Conf. Ser. Vol. 4477, Astronomical Data Analysis. SPIE, Bellingham, p. 76
Fruscione A. et al., 2006, in Silva D. R., Doxsey R. E., eds, Proc. SPIE Conf. Ser. Vol. 6270, Observatory Operations: Strategies, Processes, and Systems. SPIE, Bellingham, p. 62701V
Fukuchi H. et al., 2022, ApJ, 940, 7
Ghizzardi S. et al., 2021, A&A, 646, A92
Hardcastle M. J., Evans D. A., Croston J. H., 2006, MNRAS, 370, 1893
Hogan M. T., McNamara B. R., Pulido F., Nulsen P. E. J., Russell H. R., Vantyghem A. N., Edge A. C., Main R. A., 2017, ApJ, 837, 51
Hopkins P. F., Hernquist L., Cox T. J., Di Matteo T., Robertson B., Springel V., 2006, ApJS, 163, 1
Huenemoerder D. P. et al., 2011, AJ, 141, 129
Hutchings J. B., Neff S. G., 1991, AJ, 101, 2001
Ichikawa K. et al., 2019, ApJ, 870, 31
Jerius D., Donnelly R. H., Tibbetts M. S., Edgar R. J., Gaetz T. J., Schwartz D. A., Van Speybroeck L. P., Zhao P., 2000, in Truemper J. E., Aschenbach B., eds, Proc. SPIE Conf. Ser. Vol. 4012, X-Ray Optics, Instruments, and Missions III. SPIE, Bellingham, p. 17

Kalberla P. M. W., Burton W. B., Hartmann D., Arnal E. M., Bajaja E., Morras R., Pöppel W. G. L., 2005, A&A, 440, 775
Kallman T., Bautista M., 2001, ApJS, 133, 221
King A., 2016, MNRAS, 456, L109
King A., Pounds K., 2015, ARA&A, 53, 115
Kolman M., Halpern J. P., Shrader C. R., Filippenko A. V., Fink H. H., Schaeidt S. G., 1993, ApJ, 402, 514
Koss M. et al., 2017, ApJ, 850, 74
Li J., Kastner J. H., Prigozhin G. Y., Schulz N. S., Feigelson E. D., Getman K. V., 2004, ApJ, 610, 1204
McDonald M. et al., 2012, Nature, 488, 349
McDonald M., Gaspari M., McNamara B. R., Tremblay G. R., 2018, ApJ, 858, 45
McDonald M. et al., 2019, ApJ, 885, 63
McNamara B. R., Nulsen P. E. J., 2007, ARA&A, 45, 117
McNamara B. R. et al., 2000, ApJ, 534, L135
McNamara B. R. et al., 2014, ApJ, 785, 44
McNamara B. R., Russell H. R., Nulsen P. E. J., Hogan M. T., Fabian A. C., Pulido F., Edge A. C., 2016, ApJ, 830, 79
Mathur S., Weinberg D. H., Chen X., 2003, ApJ, 582, 82
Miller J. M., Bautz M. W., McNamara B. R., 2017, ApJ, 850, L3
Mingo B., Hardcastle M. J., Croston J. H., Evans D. A., Hota A., Kharb P., Kraft R. P., 2011, ApJ, 731, 21
Monroe T. R., Prochaska J. X., Tejos N., Worseck G., Hennawi J. F., Schmidt T., Tumlinson J., Shen Y., 2016, AJ, 152, 25
Mukai K., 1993, Legacy, 3, 21
Nulsen P. E. J., 1986, MNRAS, 221, 377
O'Sullivan E. et al., 2012, MNRAS, 424, 2971
Oegerle W. R. et al., 2000, ApJ, 538, L23
Onken C. A., Bian F., Fan X., Wang F., Wolf C., Yang J., 2020, MNRAS, 496, 2309
Planck Collaboration VIII, 2011, A&A, 536, A8
Plucinsky P. P., Bogdan A., Marshall H. L., Tice N. W., 2018, in den Herder J.-W. A., Nikzad S., Nakazawa K., eds, Proc. SPIE Conf. Ser. Vol. 10699, Space Telescopes and Instrumentation 2018: Ultraviolet to Gamma Ray. SPIE, Bellingham, p. 106996B
Reynolds C. S., Lohfink A. M., Babul A., Fabian A. C., Hlavacek-Larrondo J., Russell H. R., Walker S. A., 2014, ApJ, 792, L41
Ruiz A., Risaliti G., Nardini E., Panessa F., Carrera F. J., 2013, A&A, 549, A125
Russell H. R., Sanders J. S., Fabian A. C., 2008, MNRAS, 390, 1207
Russell H. R., Fabian A. C., Sanders J. S., Johnstone R. M., Blundell K. M., Brandt W. N., Crawford C. S., 2010, MNRAS, 402, 1561
Russell H. R., McNamara B. R., Edge A. C., Hogan M. T., Main R. A., Vantyghem A. N., 2013, MNRAS, 432, 530
Russell H. R. et al., 2017, ApJ, 836, 130
Russell H. R., Fabian A. C., McNamara B. R., Miller J. M., Nulsen P. E. J., Piotrowska J. M., Reynolds C. S., 2018, MNRAS, 477, 3583
Sanders J. S., 2006, MNRAS, 371, 829
Sanders J. S., Fabian A. C., 2007, MNRAS, 381, 1381
Schindler J.-T. et al., 2021, ApJ, 906, 12
Siemiginowska A., Burke D. J., Aldcroft T. L., Worrall D. M., Allen S., Bechtold J., Clarke T., Cheung C. C., 2010, ApJ, 722, 102
Sisk-Reynés J., Reynolds C. S., Matthews J. H., Smith R. N., 2022, MNRAS, 514, 2568
Smith R. K., Brickhouse N. S., Liedahl D. A., Raymond J. C., 2001, ApJ, 556, L91
Voit G. M., 2005, Rev. Mod. Phys., 77, 207
Walker S. A., Fabian A. C., Russell H. R., Sanders J. S., 2014, MNRAS, 442, 2809

This paper has been typeset from a TEX/LATEX file prepared by the author.